Piecewise-uniform homogenization of heterogeneous composites using a spatial decomposition based on inelastic micromechanics

Kevin Spilker[a], Van-Dung Nguyen[a], Laurent Adam[b], Ling Wu[a], Ludovic Noels[a,*]

[a] *Computational & Multiscale Mechanics of Materials, University of Liège, Belgium*
[b] *MSC Software Belgium SA (e-Xstream engineering)*
Rue Emile Francqui B9, B-1435 Mont-Saint-Guibert Belgium

Abstract

The homogenized mechanical response of heterogeneous, elasto-plastic composite materials is investigated by the use of the transformation field analysis (TFA), a two-scale algorithm relying on microscopically piece-wise uniform fields of internal variables. Not optimized spatial subdomain decompositions of the microscopic domain cause over-stiff composite material responses modeled by the TFA since the main characteristics of the inelastic field interactions are not well-represented. To improve mechanical predictions using the TFA approach, emerging inelastic fields were used to achieve enhanced spatial decompositions. The numerical estimation of the interaction functions between the subdomains allows the use of this TFA approach for the numerical modeling of a wide variety of composite materials without the need of any pre-determined reference stiffnesses. The new TFA approach was tested for materials with isotropic and anisotropic microstructures and various material systems, with a particular emphasis on the complex case of perfectly plastic material phases. Comparisons are drawn between the TFA modeling using elasticity-based and inelasticity-based spatial divisions and to reference full-field computations. The achieved results prove that more accurate predictions for the mechanical responses of composite materials can be found when inelastic fields are considered as the foundation of the spatial division into subdomains.

Preprint submitted to Composite Structures. formal publication on: doi: 10.1016/j.compstruct.2022.115836

Keywords: Transformation Field Analysis, Homogenization, Heterogeneous materials, Reduced order modeling, Elasto-plasticity

*Corresponding author
Email addresses: Kevin.Spilker@uliege.be (Kevin Spilker), VanDung.Nguyen@uliege.be (Van-Dung Nguyen), laurent.adam@Hexagon.com (Laurent Adam), l.wu@ulg.ac.be (Ling Wu), l.noels@ulg.ac.be (Ludovic Noels)

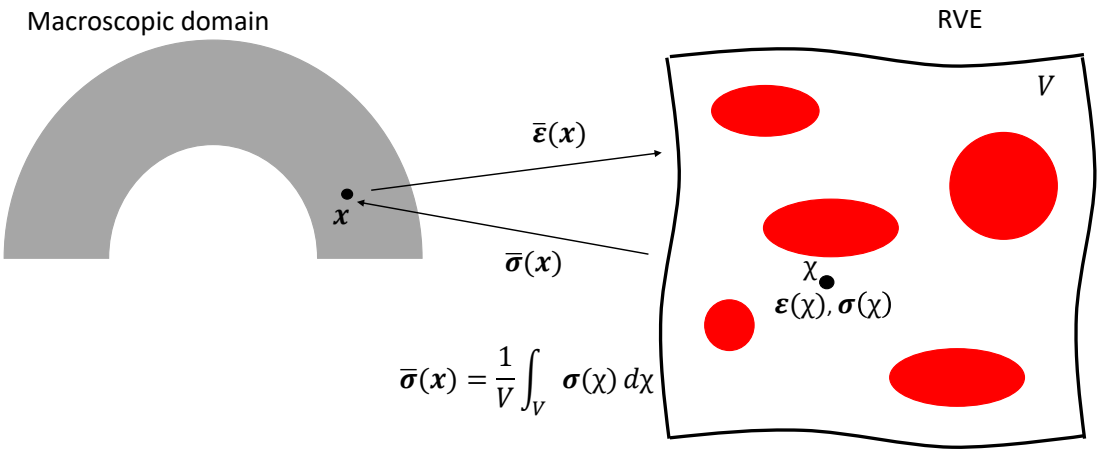

Figure 1: Schematic demonstration of full-field homogenization approach for a composite RVE subjected to a boundary problem expressed by an overall strain $\bar{\boldsymbol{\varepsilon}}(\boldsymbol{x})$, where the overall stress response $\bar{\boldsymbol{\sigma}}(\boldsymbol{x})$ follows from the consideration of local fields, for any material point $\boldsymbol{x}$ of the macroscopic boundary value problem.

1. Introduction

In recent years, the need for numerical modeling of materials with complex heterogeneous microstructures, including composite materials, has been in increasing demand in many engineering areas. Engineered composite materials have a microstructure with varying distribution, size and shape of the material constituents at the microscopic scale resulting from the manufacturing process. Many other types of materials of interest in engineering disciplines have a naturally heterogeneous microstructure (polycrystalline materials, geomaterials, biomaterials and more). Performing an accurate mechanical analysis of a macroscopic structure requires an analysis of the underlying microstructure, since mechanical processes affecting the materials macroscopic response like plasticity and damage originate on the micro-scale. This kind of simulations, analysing the macroscopic material response by taking into account microscopic processes, are known as multi-scale simulations, see (Kanouté et al., 2009; Charalambakis, 2010; Geers et al., 2010; Saeb et al., 2016; Geers et al., 2017; Yvonnet, 2019, e.g.). In homogenization-based multi-scale methods, the deformation state at one point of the macroscopic domain constitutes a new boundary value problem (BVP) applied on a microscopic domain assumed to contain all microscopic features and called representative volume element (RVE).

Analytical and semi-analytical methods in the non-linear range rely on the definition of a so-called linear comparison composite (LCC) with linear properties being equivalent to the linearized effective properties of the actual non-linear composite (Ponte Castaeda, 1992, 1996). Variational approaches (Ponte Castaeda, 2002a,b; Lopez-Pamies and Castaeda, 2004; Lopez-Pamies et al., 2013) and the related mean-field homogenizations methods, which consider per-phase average strain and stress fields linked by so-called concentration tensors (Doghri et al., 2011; Wu et al., 2013, 2017) are formulated on the basis of this LCC. While being computationally very efficient, analytical methods and MFH schemes rely on certain

assumptions on the microstructural phase distributions and therefore have certain limitations when dealing with cases of complex heterogeneous and anisotropic microstructures, motivating the development of fully computational homogenization approaches (Fig. 1). Computational homogenization methods contain FE^2 (Feyel, 1999; Kouznetsova et al., 2001, e.g.) as well as fast Fourier transformation (FFT) based approaches (Moulinec and Suquet, 1994, 1998), in which, at the micro-scale, local constitutive equations are solved over the fully discretized integration domain. While the use of direct numerical simulations for the solution of the RVE boundary problem are able to provide a high accuracy, their computational effort is immense when dealing with complex heterogeneous microstructures due to the need of a fine discretization and therefore a large number of internal variables.

In order to make multi-scale simulations with high accuracy utilizable for a wider range of purposes, homogenization methods based on fully computational homogenization approaches ought to follow a model reduction step. Reduced order models (ROMs) consist of an offline stage which contains direct numerical simulations, providing the capability to deal with complex microstructures. Subsequently, the gathered information from the offline stage is reduced in order to consider only the essential features of the full-field problem by the means of a reduced number of internal variables. In the online stage, constitutive relations for the reduced problem are solved in order to achieve the estimated mechanical response of the overall composite.

Models can be reduced by projecting the governing equations into suitably selected subspaces defined from offline computations, leading to a reduction of the number of unknown variables by means of proper orthogonal decomposition (POD) as suggested by Yvonnet and He (2007). In this context, the equilibrium equations are projected in a basis of reduced size, and a further order reduction called hyper-reduction, see the work by Hernández et al. (2014); Soldner et al. (2017); Caicedo et al. (2019), follows to reduce the evaluation of the constitutive laws at a reduced set of points or elements.

Liu et al. (2019); Liu and Wu (2019) have developed the so-called deep material network (DMN) approach based on analytical micro-mechanics models, such as laminate theory, defining mechanistic building blocks which form a binary hierarchical topological structure. Elastic offline simulations define the parameters of the building blocks, so that the DMN can be used to predict non-linear responses. The good handling of this extrapolation was theoretically explained by Gajek et al. (2020). Nguyen and Noels (2022b) have provided an efficient implementation, Wu et al. (2021) have used complex micro-mechanical models such as MFH in the mechanistic building blocks for woven composite materials, and Nguyen and Noels (2022a) have replaced the micro-mechanical models in the building blocks by interactions which obey the Hill-Mandel condition.

ROMs can also be based on micro-mechanics models involving much less variables, as in the transformation field analysis (TFA) pioneered by Dvorak (1992) first for two-phase and following for multi-phase composite materials. The TFA is based on the spatial division of the RVE into subdomains and the separation of local elastic and inelastic fields, alternatively referred to as transformation fields or eigenfields. Local elastic interaction functions due to transformation fields are provided by local coupling relations. The interaction functions make the TFA applicable as a ROM method using a spatial division into subdomains and

assuming piecewise uniform fields of internal variables inside the single subdomains (Dvorak, 1990). Considering the objective of a ROM application, local interactions are computed by full-field simulations in the offline stage and mean interactions between chosen subdomains are used to solve the TFA constitutive equations in the online stage. Applying the TFA for the case of a microstructure consisting of two phases and using one subdomain per phase can be considered as an actual MFH approach. But since no restrictions for the number of phases and their geometry exist, the TFA can be regarded as a generalized MFH method. After it was recognized that the TFA with a low number of subdomains clearly overestimates the inelastic stress response of a composite and that the reason are insufficient interaction effects of the mean inelastic fields, Chaboche et al. (2001) introduced a plastic correction method based on a comparison to the Hill strain concentration tensors in a two-phase solid. A comparison to different MFH formulations is given by Chaboche et al. (2005). Starting from the asymptotic homogenization mathematical formalism, Fish et al. (1997) have formulated the response of elasto-plastic composites from eigenstrain fields discretized using piecewise uniform approximations on the RVE, yielding a formulation bearing some similarities with the TFA approach. Michel and Suquet (2003, 2004, 2009) introduced the non-uniform TFA (NTFA) with the goal of achieving better estimates for the composite mechanical response by extending the TFA to an integration of global heterogeneous plastic fields. The non-uniform fields are represented by a number of dominant plastic modes acting as global shape functions, extracted from inelastic offline simulations. The mode activity in the online stage was controlled by and restricted to basic evolution laws. The global NTFA was extended to the computation of evolution equations of internal variables derived from variational principles by Fritzen and Leuschner (2013), allowing the use of the NTFA for all generalized standard material (GSM) classes, and subsequently to the incorporation of second-order potentials (Michel and Suquet, 2016).

Based on the NTFA considering a number of global inelastic modes, a strategy was introduced building on a non-uniform distribution of internal variables over selected subdomains (Sepe et al., 2013). Only elastic offline simulations are required, but evolution equations during the online stage are evaluated at all microscopic integration points resulting in significantly increased computational efforts. A further development incorporates the use of stress instead of inelastic strain shape functions in each subdomain and the solution of weak-form relations for the subdomains, reducing computational requirements for the online stage (Covezzi et al., 2016). A recent extension of this piecewise non-uniform TFA using global inelastic modes combines it with the domain decomposition using a statistical clustering approach based on different deformation conditions (Ri et al.). The computed overall behavior of the RVE follows purely from the constitutive relations in the subdomains, allowing the computation of the mechanical response for all kinds of heterogeneous material systems.

Another ROM approach relying on the assumption of piecewise uniform fields of internal variables is the self-consistent clustering analysis (SCCA) by Liu et al. (2016, 2018). The offline stage consists of elastic pre-simulations and a clustering approach, dividing the RVE into subdomains purely based on elastic strain distributions. The SCCA formulation bases on interactions between the subdomains by making use of influence functions of the local transformation field. The influence functions are expressed by the Green's function of a

selected isotropic and homogeneous material. The Lippmann-Schwinger equation is used as coupling equation between the clusters in the online stage to solve the overall problem, while the internal variables are considered uniform per subdomain. The local transformation field during the online stage does not follow from the classical tangent relation, but on a homogeneous and isotropic reference stiffness, being either chosen as constant or updated during the online stage using a self-consistent formulation. We note the assumption of the isotropic character of the reference material when using the Green's function in the SCCA method. A related and recently presented approach of this class relying on piecewise uniform fields and the integration of an isotropic and homogeneous reference stiffness is the Hashin-Shtrikman type finite element method (HSFE) used as a ROM technique for non-linear-elastic materials by Wulfinghoff et al. (2018); Cavaliere et al. (2020). It was later applied for elasto-plastic materials by Castrogiovanni et al. (2021). For this method, a similar clustering approach based on elastic strain distributions is used to discretize the RVE into subdomains. The overall RVE response is achieved by solving a coupling relation between the subdomains in the online stage. Similarly to the previously mentioned approach, the incremental local transformation field for the subdomains during the online stage does not follow purely from the local subdomain properties, but is evaluated by the use of the chosen isotropic and homogeneous reference stiffness, being defined as a secant stiffness.

The paper at hand presents the uniform TFA approach used as a ROM homogenization technique suitable for the purpose of multi-scale modeling of random-structured inelastic composite materials during loading-unloading conditions even in cases of very localized plasticity. To this end, the following ingredients are considered

- In order for the spatial division into subdomains to be well-representative of the inelastic micromechanical deformation patterns inside the material, this subdivision is based on plastic strain tensor distributions obtained by selected offline loading conditions;
- In order to account for plastic field fluctuations inside each subdomain and to allow for an additional acceleration of the convergence towards full-field results, a sensible correction approach for the use of piecewise uniform field approaches is constructed from the inelastic field fluctuations within each subdomain observed during the offline stage;
- In order to remain general for different microstructures, the local interaction functions are evaluated numerically.

As a result, the TFA constitutive relations rely purely on local properties and therefore do not require any pre-assumptions for an isotropic and homogeneous reference material, which distinguishes the TFA from the two aforementioned approaches SCCA and HSFE. Furthermore, the need of any local shape functions is waived using the uniform TFA, significantly reducing the memory and computational requirements with respect to the mentioned NTFA techniques. The method using a reasonable number of subdomains provides overall RVE responses being in good accuracy with full-field simulations, considered as "real" solutions. For elasto-plastic phase responses exhibiting a hardening behavior, very low numbers of

subdomains ($\leq$ 20) are sufficient to provide accurate results, while the most demanding case of elastic inclusions in a perfectly plastic matrix requires a few hundreds of subdomains. In particular improved results in comparison with the use of the conventional spatial decomposition based on elasticity are achieved.

This paper is structured as follows: Section 2 presents the analytical TFA approach by means of an overview of the constitutive relations demonstrated in a continuous medium before translating them into the discretized form using subdomains. Section 3 contains an overview of the numerical aspects of computational homogenization, before all numerical steps to achieve the solution for the mechanical RVE response by using the TFA as a ROM approach are presented. The elasticity-based and inelasticity-based reductions from a discretized full-field problem to a reduced problem are described. A new approach is proposed for the incorporation of numerically determined plastic field fluctuations inside the subdomains in order to achieve improved homogenized responses, making use of statistical measures of plastic field inhomogeneities gathered in the offline stage. Finally, the iterative procedure using the TFA algorithm to solve the RVE problem in the online stage is described. Section 4 displays homogenized stress responses resulting from the TFA implementations in comparison to reference full-field computations. The mechanical behavior of composite materials with various micro-structures and material systems, in particular the complex case of elastic inclusions in a matrix phase with a perfectly plastic behavior, are accurately represented using the developed enhanced spatial subdivision for low to moderate volume fraction of inclusions. In Section 5, concluding remarks of this work and possible future contributions on this subject are pointed out.

2. Constitutive relations in a heterogeneous medium

2.1. Micromechanics in a heterogeneous continuous medium

Considering a representative volume element (RVE) V with the volume

$$|V| = \int_V \mathrm{d}\boldsymbol{\chi}, \tag{1}$$

inside a heterogeneous medium, the overall strain and stress of the material body V are given as

$$\overline{\boldsymbol{\varepsilon}} = \frac{1}{|V|} \int_V \boldsymbol{\varepsilon}(\boldsymbol{\chi}) \mathrm{d}\boldsymbol{\chi} \tag{2}$$

and

$$\overline{\boldsymbol{\sigma}} = \frac{1}{|V|} \int_V \boldsymbol{\sigma}(\boldsymbol{\chi}) \mathrm{d}\boldsymbol{\chi}. \tag{3}$$

The local stress field $\boldsymbol{\sigma}(\boldsymbol{\chi}, t)$ at the time t follows from a constitutive model

$$\boldsymbol{\sigma}(\boldsymbol{\chi}, t) = f\big(\boldsymbol{\varepsilon}(\boldsymbol{\chi}, t), z(\boldsymbol{\chi}, t'), \forall t' \leq t\big)\,, \tag{4}$$

with the internal state variables $z(\boldsymbol{\chi}, t')$, where the dependence on the history is expressed through t' with $t' \leq t$.

If the state of the material domain V is elastic, the local strain field $\boldsymbol{\varepsilon}(\boldsymbol{\chi})$ inside the body can be expressed as

$$\boldsymbol{\varepsilon}(\boldsymbol{\chi}) = \mathbb{A}^{\mathrm{el}}(\boldsymbol{\chi}) : \overline{\boldsymbol{\varepsilon}}, \quad \boldsymbol{\chi} \in V \tag{5}$$

with the local elastic strain concentration tensor $\mathbb{A}^{\mathrm{el}}(\boldsymbol{\chi})$. The local stress field in Eq. (4) is given as

$$\boldsymbol{\sigma}(\boldsymbol{\chi}) = \mathbb{C}^{\mathrm{el}}(\boldsymbol{\chi}) : \boldsymbol{\varepsilon}(\boldsymbol{\chi}), \quad \boldsymbol{\chi} \in V, \tag{6}$$

with the local elastic stiffness tensor $\mathbb{C}^{\mathrm{el}}(\boldsymbol{\chi})$. The expression of the overall strain and stress in Eqs. (2) and (3) can be reformulated to

$$\overline{\boldsymbol{\varepsilon}} = \left[\frac{1}{|V|}\int_V \mathbb{A}^{\mathrm{el}}(\boldsymbol{\chi})\,\mathrm{d}\boldsymbol{\chi}\right] : \overline{\boldsymbol{\varepsilon}} \tag{7}$$

and

$$\overline{\boldsymbol{\sigma}} = \left[\frac{1}{|V|}\int_V \mathbb{C}^{\mathrm{el}}(\boldsymbol{\chi}) : \mathbb{A}^{\mathrm{el}}(\boldsymbol{\chi})\,\mathrm{d}\boldsymbol{\chi}\right] : \overline{\boldsymbol{\varepsilon}}, \tag{8}$$

the latter leading to the expression for the overall elastic stiffness

$$\overline{\mathbb{C}}^{\mathrm{el}} = \frac{d\overline{\boldsymbol{\sigma}}}{d\overline{\boldsymbol{\varepsilon}}} = \frac{1}{|V|}\int_V \mathbb{C}^{\mathrm{el}}(\boldsymbol{\chi}) : \mathbb{A}^{\mathrm{el}}(\boldsymbol{\chi})\mathrm{d}\boldsymbol{\chi}. \tag{9}$$

The non-linear behavior of the material is accounted for by a consideration of local eigenstress field $\boldsymbol{\sigma}^*(\boldsymbol{\chi})$, or corresponding local eigenstrain field

$$\boldsymbol{\varepsilon}^*(\boldsymbol{\chi}) = -\mathbb{S}^{\mathrm{el}}(\boldsymbol{\chi}) : \boldsymbol{\sigma}^*(\boldsymbol{\chi})\,, \tag{10}$$

with the local elastic compliance

$$\mathbb{S}^{\mathrm{el}}(\boldsymbol{\chi}) = \mathbb{C}^{\mathrm{el}}(\boldsymbol{\chi})^{-1}, \tag{11}$$

in an elastic medium, leading to the definition of the local strain field

$$\boldsymbol{\varepsilon}(\boldsymbol{\chi}) = \boldsymbol{\varepsilon}^{\mathrm{el}}(\boldsymbol{\chi}) + \boldsymbol{\varepsilon}^*(\boldsymbol{\chi}), \tag{12}$$

composed of an elastic portion $\boldsymbol{\varepsilon}^{\mathrm{el}}(\boldsymbol{\chi})$ and the eigenstrain field $\boldsymbol{\varepsilon}^*(\boldsymbol{\chi})$. The constitutive relation in Eq. (4) is alternatively stated under the form

$$\begin{aligned}\boldsymbol{\sigma}(\boldsymbol{\chi}) &= \mathbb{C}^{\mathrm{el}}(\boldsymbol{\chi}) : \big(\boldsymbol{\varepsilon}(\boldsymbol{\chi}) - \boldsymbol{\varepsilon}^*(\boldsymbol{\chi})\big) \\ &= \mathbb{C}^{\mathrm{el}}(\boldsymbol{\chi}) : \boldsymbol{\varepsilon}(\boldsymbol{\chi}) + \boldsymbol{\sigma}^*(\boldsymbol{\chi})\,,\end{aligned} \tag{13}$$

implying that the eigenstrains belong to the internal state variables $z(\boldsymbol{\chi})$ in Eq. (4).

In the concept of the TFA, the local strain field inside V is directly connected to the local eigenstrain field $\boldsymbol{\varepsilon}^*(\boldsymbol{\chi})$. In the case of a vanishing overall strain $\overline{\boldsymbol{\varepsilon}} = 0$, the local strain field can be expressed as

$$\boldsymbol{\varepsilon}(\boldsymbol{\chi}) = \mathbb{D}(\boldsymbol{\chi}, \boldsymbol{\chi}') : \boldsymbol{\varepsilon}^*(\boldsymbol{\chi}') \quad \boldsymbol{\chi}, \boldsymbol{\chi}' \in V\,, \tag{14}$$

with the interaction function $\mathbb{D}(\boldsymbol{\chi}, \boldsymbol{\chi}')$, estimating the effect of an eigenstrain field $\boldsymbol{\varepsilon}^*(\boldsymbol{\chi}')$ on the strain at $\boldsymbol{\chi}$ (Dvorak, 1992). Subject of this paper is the numerical determination of the interaction function $\mathbb{D}(\boldsymbol{\chi}, \boldsymbol{\chi}')$ in a heterogeneous and finite material domain. An existing eigenstrain field in the material domain under a vanishing overall strain $\overline{\boldsymbol{\varepsilon}} = |V|^{-1} \int_V \boldsymbol{\varepsilon}(\boldsymbol{\chi}) \mathrm{d}\boldsymbol{\chi} = 0$ leads to the expression

$$\int_V \boldsymbol{\varepsilon}(\boldsymbol{\chi}) \, \mathrm{d}\boldsymbol{\chi} = \int_V \mathbb{D}(\boldsymbol{\chi}, \boldsymbol{\chi}') : \boldsymbol{\varepsilon}^*(\boldsymbol{\chi}') \, \mathrm{d}\boldsymbol{\chi} = \mathbf{0}, \tag{15}$$

implying for arbitrary eigenstrain distributions $\boldsymbol{\varepsilon}^*(\boldsymbol{\chi}')$ the condition

$$\int_V \mathbb{D}(\boldsymbol{\chi}, \boldsymbol{\chi}') \, \mathrm{d}\boldsymbol{\chi} = \mathbf{0} \, . \tag{16}$$

Considering now a general mechanical problem as given in Eq. (12), the resulting local strain field is given as the superposition of the two particular problems presented above

1. the material with an overall strain $\overline{\boldsymbol{\varepsilon}} \neq 0$ in the absence of an eigenstrain field,

2. the material containing an eigenstrain field $\boldsymbol{\varepsilon}^*(\boldsymbol{\chi}) \neq 0$ and a vanishing overall strain,

expressed by the superposition of the Eqs. (5) and (14), yielding

$$\boldsymbol{\varepsilon}(\boldsymbol{\chi}) = \mathbb{A}^{\mathrm{el}}(\boldsymbol{\chi}) : \overline{\boldsymbol{\varepsilon}} + \mathbb{D}(\boldsymbol{\chi}, \boldsymbol{\chi}') : \boldsymbol{\varepsilon}^*(\boldsymbol{\chi}'), \quad \boldsymbol{\chi} \in V. \tag{17}$$

This equation provides an analytical field relation and a coupling relation between the microscopic and macroscopic material scales.

2.2. Discretized subdomain consideration of the continuous problem

The continuum TFA form presented in Section 2.1 can be formulated in a reduced form considering a division of the continuous domain V into subdomains V_r. Average quantities over the subdomains with the volumes

$$|V_r| = \int_{V_r} \mathrm{d}\boldsymbol{\chi} \tag{18}$$

are considered instead of local quantities and a uniform distribution of all internal state variables is assumed inside the K subdomains denoted by the index r. The piecewise uniform fields of local variables $\beta(\boldsymbol{\chi})$ are expressed by

$$\beta(\boldsymbol{\chi}) = \sum_{r=1}^{K} \beta_r \xi_r(\boldsymbol{\chi}) \tag{19}$$

with the per-subdomain r constant value β_r and the spatial distribution function

$$\xi_r(\boldsymbol{\chi}) = \begin{cases} 1 & , \boldsymbol{\chi} \in V_r \\ 0 & , \text{otherwise,} \end{cases} \tag{20}$$

automatically implying

$$\beta_r = \frac{1}{|V_r|} \int_{V_r} \beta(\boldsymbol{\chi}) \mathrm{d}\boldsymbol{\chi}, \tag{21}$$

meaning that the uniform quantities of a subdomain equal the averaged quantities over the subdomain. Using Eq. (21), all local variables can be written in their discrete reduced form.

2.2.1. Total formulation

The overall homogenized strain and stress of the RVE are given as

$$\overline{\boldsymbol{\varepsilon}} = \sum_{r=1}^{K} \upsilon_r \boldsymbol{\varepsilon}_r \tag{22}$$

and

$$\overline{\boldsymbol{\sigma}} = \sum_{r=1}^{K} \upsilon_r \boldsymbol{\sigma}_r, \tag{23}$$

where $\upsilon_r = |V_r|/|V|$ and the subdomain strains and stresses read

$$\boldsymbol{\varepsilon}_r = \boldsymbol{\varepsilon}_r^{\mathrm{el}} + \boldsymbol{\varepsilon}_r^{*} \tag{24}$$

and

$$\begin{aligned} \boldsymbol{\sigma}_r &= \mathbb{C}_r^{\mathrm{el}} : (\boldsymbol{\varepsilon}_r - \boldsymbol{\varepsilon}_r^{*}) \\ &= \mathbb{C}_r^{\mathrm{el}} : \boldsymbol{\varepsilon}_r + \boldsymbol{\sigma}_r^{*}. \end{aligned} \tag{25}$$

In the absence of an eigenstrain field, subdomain strains and stresses are given as

$$\boldsymbol{\varepsilon}_r = \mathbb{A}_r^{\mathrm{el}} : \overline{\boldsymbol{\varepsilon}} \tag{26}$$

and

$$\boldsymbol{\sigma}_r = \mathbb{C}_r^{\mathrm{el}} : \mathbb{A}_r^{\mathrm{el}} : \overline{\boldsymbol{\varepsilon}} \tag{27}$$

with the piecewise uniform subdomain stiffness $\mathbb{C}_r^{\mathrm{el}}$. The reduced form of Eq. (7),

$$\sum_{r=1}^{K} \upsilon_r \mathbb{A}_r^{\mathrm{el}} = \mathbb{I}, \tag{28}$$

is implied in order to satisfy Eq. (22). The expression for the subdomain stresses in Eq. (27) leads to the reduced equivalent of the overall elastic stiffness in Eq. (9) formulated as

$$\overline{\mathbb{C}}^{\mathrm{el}} = \sum_{r=1}^{K} \upsilon_r \mathbb{C}_r^{\mathrm{el}} : \mathbb{A}_r^{\mathrm{el}}. \tag{29}$$

Considering the case of possible existing eigenstrains $\boldsymbol{\varepsilon}_r^{*}$ in the subdomains r, the elastic eigenstress-eigenstrain relation following Eq. (10) reads

$$\boldsymbol{\varepsilon}_r^{*} = -\mathbb{S}_r^{\mathrm{el}} : \boldsymbol{\sigma}_r^{*} \tag{30}$$

with the subdomain elastic compliance $\mathbb{S}_r^{\mathrm{el}}$. The discretized continuum relation in Eq. (14) for the subdomains in the presence of eigenstrains and the absence of an overall strain reads

$$\boldsymbol{\varepsilon}_r = \sum_{s=1}^{K} \mathbb{D}_{rs} : \boldsymbol{\varepsilon}_s^{*}, \quad \text{at} \quad \overline{\boldsymbol{\varepsilon}} = \mathbf{0} \tag{31}$$

with the eigenstrain interaction tensor $\mathbb{D}_{rs}$, accounting for elastic influence effects of the eigenstrain in the subdomains s on the strain in subdomain r. For Eq. (22) to remain true for all possible eigenstrain distributions over the subdomains, the condition in Eq. (16) in its reduced form

$$\sum_{r=1}^{K} v_r \mathbb{D}_{rs} = \mathbf{0} \tag{32}$$

is to be satisfied (Eq. (50.1) in Dvorak (1992)).

The solution of the discrete total non-linear problem follows from a superposition of the two distinct problems of the material body in elasticity (Eq. (26)) and the case of a vanishing overall strain and occurring eigenstrain field (Eq. (31)) as

$$\boldsymbol{\varepsilon}_r = \mathbb{A}_r^{\mathrm{el}} : \overline{\boldsymbol{\varepsilon}} + \sum_{s=1}^{K} \mathbb{D}_{rs} : \boldsymbol{\varepsilon}_s^*, \tag{33}$$

being the reduced form of the micro-macro coupling relation in Eq. (17).

2.2.2. Incremental formulation

In the following, history-dependent behavior of the material is considered. The rates of the above equations integrated over a discrete time interval lead to the TFA coupling relation in its incremental formulation

$$\Delta\boldsymbol{\varepsilon}_r = \mathbb{A}_r^{\mathrm{el}} : \Delta\overline{\boldsymbol{\varepsilon}} + \sum_{s=1}^{K} \mathbb{D}_{rs} : \Delta\boldsymbol{\varepsilon}_s^*. \tag{34}$$

The overall strain and stress increments read

$$\Delta\overline{\boldsymbol{\varepsilon}} = \sum_{r=1}^{K} v_r \Delta\boldsymbol{\varepsilon}_r \tag{35}$$

and

$$\Delta\overline{\boldsymbol{\sigma}} = \sum_{r=1}^{K} v_r \Delta\boldsymbol{\sigma}_r. \tag{36}$$

The incremental strain-stress relation of the subdomains reads

$$\Delta\boldsymbol{\sigma}_r = \mathbb{C}_r^{\mathrm{el}} : (\Delta\boldsymbol{\varepsilon}_r - \Delta\boldsymbol{\varepsilon}_r^*). \tag{37}$$

The eigenstrain increment $\Delta\boldsymbol{\varepsilon}_r^*$, its derivative $\partial\Delta\boldsymbol{\varepsilon}_r^*/\partial\boldsymbol{\varepsilon}_r$ and the per-subdomain uniform tangent operator

$$\mathbb{C}_r^{\mathrm{tan}} = \frac{\partial\Delta\boldsymbol{\sigma}_r}{\partial\boldsymbol{\varepsilon}_r}, \tag{38}$$

expressing the incremental response of the subdomains, follow from the local constitutive law as detailed in the next section.

2.3. Local constitutive relations

In this work, local inelastic stress responses and the local tangent stiffnesses follow from the classical J_2-plasticity model. In this section, the material point denoted by $\boldsymbol{\chi}$ and the subscript r referring to the subdomain V_r are omitted in the equations. The yield function for isotropic hardening

$$f^{\mathrm{Y}}(\boldsymbol{\sigma}, p) = \sigma^{\mathrm{eq}} - \sigma^{\mathrm{Y}}(p) \leq 0 \tag{39}$$

is to be fulfilled in order to satisfy the von Mises law, where p is the accumulated equivalent plastic strain. In the yield function $f^{\mathrm{Y}}(\boldsymbol{\sigma}, p)$, the current yield stress reads

$$\sigma^{\mathrm{Y}} = \sigma^{\mathrm{Y0}} + R(p), \tag{40}$$

with the initial yield stress σ^{Y0} and the hardening stress $R(p)$ following from the expression of the governing hardening law and the accumulated equivalent plastic strain p. The equivalent plastic strain increment reads

$$\Delta p = \sqrt{\frac{2}{3}\Delta\boldsymbol{\varepsilon}^{\mathrm{p}} : \Delta\boldsymbol{\varepsilon}^{\mathrm{p}}} \tag{41}$$

with the incremental plastic strain tensor

$$\Delta\boldsymbol{\varepsilon}^{\mathrm{p}} = \Delta p \boldsymbol{N}, \tag{42}$$

where $\boldsymbol{N} = \partial f^{\mathrm{Y}} / \partial \boldsymbol{\sigma}$ is the plastic flow direction. The eigenstrain $\boldsymbol{\varepsilon}^*$ considered in Sections 2.1 and 2.2 corresponds to the plastic strain tensor as $\boldsymbol{\varepsilon}^{\mathrm{p}}$.

The second part is the current equivalent von Mises stress

$$\sigma^{\mathrm{eq}} = \sqrt{3J_2(\boldsymbol{s})}, \tag{43}$$

with the second invariant

$$J_2(\boldsymbol{s}) = \frac{1}{2}\,\boldsymbol{s} : \boldsymbol{s} \tag{44}$$

of the deviatoric stress

$$\boldsymbol{s} = \mathrm{dev}(\boldsymbol{\sigma}). \tag{45}$$

The resolution of the incremental problem at one current time step follows a predictor-corrector scheme, starting from the assumption of no occurring plastic flow, and hence the incremental ("predicted") elastic trial stress state

$$\boldsymbol{\sigma}^{\mathrm{tr}} = \boldsymbol{\sigma}_n + \mathbb{C}^{\mathrm{el}} : \Delta\boldsymbol{\varepsilon}, \tag{46}$$

where $\boldsymbol{\sigma}_n$ is the stress solved at the former time step, and the corresponding yield function

$$f^{\mathrm{Y}}(\boldsymbol{\sigma}, \boldsymbol{\varepsilon}^{\mathrm{p}}) = \sigma^{\mathrm{tr,eq}} - \sigma^{\mathrm{Y}} \tag{47}$$

with $\sigma^{\mathrm{tr,eq}} = \sqrt{3J_2(\boldsymbol{s}^{\mathrm{tr}})}$. In case of $f^{\mathrm{Y}} > 0$, the scheme yields, by solving the above equations in order to satisfy the condition (39), the resulting plastic flow in Eq. (42), where the flow direction is given as

$$\boldsymbol{N} = \frac{3}{2}\frac{\boldsymbol{s}^{\mathrm{tr}}}{\sigma^{\mathrm{tr,eq}}}. \tag{48}$$

The plastic flow maps the trial stress state in Eq. (46) on to the corresponding yield surface, finally providing the ("corrected") stress state as

$$\boldsymbol{\sigma} = \boldsymbol{\sigma}^{\mathrm{tr}} - \mathbb{C}^{\mathrm{el}} : \Delta\boldsymbol{\varepsilon}^{\mathrm{p}}. \tag{49}$$

In case of isotropic plasticity, Eq. (49) can be expressed as

$$\boldsymbol{\sigma} = \boldsymbol{\sigma}^{\mathrm{tr}} - 2G^{\mathrm{el}}\Delta\boldsymbol{\varepsilon}^{\mathrm{p}}, \tag{50}$$

with the elastic shear modulus of the material G^{el}. The derivative of the plastic strains reads

$$\frac{\partial \Delta\boldsymbol{\varepsilon}^{\mathrm{p}}}{\partial \boldsymbol{\varepsilon}} = \frac{2G^{\mathrm{el}}}{h}\boldsymbol{N}\otimes\boldsymbol{N} + 2G^{\mathrm{el}}\frac{\Delta p}{\sigma^{\mathrm{tr,eq}}}\left(\frac{3}{2}\mathbb{I}^{\mathrm{dev}} - \boldsymbol{N}\otimes\boldsymbol{N}\right), \tag{51}$$

and the consistent tangent stiffness reads

$$\begin{aligned}\mathbb{C}^{\mathrm{tan}} = \frac{\partial \Delta\boldsymbol{\sigma}}{\partial \boldsymbol{\varepsilon}} &= \mathbb{C}^{\mathrm{el}} - 2G^{\mathrm{el}}\frac{\partial \Delta\boldsymbol{\varepsilon}^{\mathrm{p}}}{\partial \boldsymbol{\varepsilon}} \\ &= \mathbb{C}^{\mathrm{el}} - \frac{(2G^{\mathrm{el}})^2}{h}\boldsymbol{N}\otimes\boldsymbol{N} - (2G^{\mathrm{el}})^2\frac{\Delta p}{\sigma^{\mathrm{tr,eq}}}\left(\frac{3}{2}\mathbb{I}^{\mathrm{dev}} - \boldsymbol{N}\otimes\boldsymbol{N}\right),\end{aligned} \tag{52}$$

where

$$h = 3G^{\mathrm{el}} + \partial R/\partial p. \tag{53}$$

Details of the computations in Eqs. (51) and (52) are given in Appendix A.

3. Numerical methodology

Using a full-field homogenization technique to compute the overall response of the RVE, a system of equations over the whole material domain V inside the RVE is solved. ROM techniques considering a reduced problem instead can be used as surrogate models replacing the often computationally heavy full-field homogenization methods. The TFA formulation Eq. (34) is developed in this work to be used as such a ROM surrogate modeling approach. This is achieved by using averaged variables over subdomains containing the microscopic material points that follow a similar deformation behavior.

This section provides first in Section 3.1 a summary of the fundamental rules to be satisfied using computational homogenization schemes. Following, the details of the model order reduction procedure through the spatial division based on elastic and inelastic fields is described in Section 3.2. A TFA correction scheme based on in-subdomain heterogeneities with the goal of providing improved results is proposed in Section 3.3. Finally, the solution details of the reduced mechanical problem are presented in Section 3.4.

3.1. Computational Homogenization

The homogenized strain-stress response of a RVE can be achieved by solving a BVP computationally over the discretized microscopic domain using full-field approaches like the FE method. In the absence of dynamic effects, the equilibrium equations

$$\begin{cases} \nabla \cdot \boldsymbol{\sigma} = 0 & \forall \boldsymbol{\chi} \in V \,, \\ \boldsymbol{n} \cdot \boldsymbol{\sigma} = \boldsymbol{t} & \forall \boldsymbol{\chi} \in \partial V \,, \end{cases} \tag{54}$$

are to be satisfied at all microscopic material points $\boldsymbol{\chi}$, where $\boldsymbol{\sigma} = \boldsymbol{\sigma}(\boldsymbol{\chi})$ is the Cauchy stress tensor and $\boldsymbol{t} = \boldsymbol{t}(\boldsymbol{\chi})$ is the surface traction in the direction of the outward unit normal $\boldsymbol{n} = \boldsymbol{n}(\boldsymbol{\chi})$ on the RVE boundary ∂V. Homogenized quantities over the full discretized domain (or "overall" quantities) are expressed as

$$\overline{\beta} = \frac{1}{|V|} \int_V \beta(\boldsymbol{\chi}) \mathrm{d}\boldsymbol{\chi} \,. \tag{55}$$

The problem of computational homogenization is schematically presented in Fig. 1, where the homogenized strain-stress response is extracted from the resolution of the BVP over the discretized RVE with a prescribed overall strain using the FE method. A requirement for the multi-scale modeling of finite domains using direct numerical simulations (DNS) is the satisfaction of the Hill-Mandel condition, providing the energy consistency between the different scales. The base for the computational homogenization of finite domains was set up by the work done by Peric et al. (2010); Geers et al. (2010); Saeb et al. (2016). The consideration of volume elements with sizes below the statistical representation was treated by Ostoja-Starzewski et al. (2007), where it is shown that presented formalism for the computational homogenization of statistical volume elements still hold for smaller domains. For the two-dimensional direct numerical simulations performed in this work using the FE method, periodic boundary conditions (PBCs) were applied. The displacement field imposed by PBCs satisfies the weak form of the equilibrium condition in Eq. (54) and the Hill-Mandel condition as detailed by Nguyen et al. (2017).

3.2. Offline stage: reduction of the full field problem

In order to use the TFA as a ROM technique for the mechanical homogenization, the microscopic points of the RVE are divided into several subdomains and over the subdomains averaged quantities

$$\beta_r = \frac{1}{|V_r|} \int_{V_r} \beta(\boldsymbol{\chi}) \mathrm{d}\boldsymbol{\chi} \tag{56}$$

are considered. For the case of more than one material phase, each phase is subdivided separately. A more refined discretization than simply using one subdomain per material phase is achieved by selecting a local variable $\beta(\boldsymbol{\chi})$ and analyzing its distribution in the corresponding phase. The microscopic points are then divided based on the local similarity of the selected quantity. Thereby the subdivisions are not necessarily coherent in space. In the following, RVE decomposition based on elastic and inelastic strain distributions are

presented. A k-means clustering approach as proposed by Liu et al. (2016) is used to divide all microscopic points in the full-field domain into groups based on the similarity of their elastic or inelastic strain tensors (MacQueen, 1967). In order to achieve accurate mechanical local fields for the spatial partitioning, certain discrete numerical full field simulations are performed in the offline stage. The number and type of the full field pre-simulations depend on the chosen variable to be characterized. In the following, all N_r local data points constituting the subdomain volume V_r are denoted by the index i, expressed as

$$\boldsymbol{\chi}_i \in V_r, \quad i = 1, ..., N_r \,. \tag{57}$$

After the spatial decomposition, interaction tensors between the subdomains are determined. The division of all local material points into the subdomains is performed phase-wise, and in the following, the material phases are denoted by the index Ω.

3.2.1. Subdomain decomposition based on local elastic strain fields

The local elastic strain concentration tensors $\mathbb{A}^{\mathrm{el}}(\boldsymbol{\chi})$ in an RVE link the strain at any material point $\boldsymbol{\chi}$ in the microscopic domain inside the RVE, considered in elasticity and without any eigenfields, to the overall strain of the RVE following from Eq. (5) as

$$\boldsymbol{\varepsilon}(\boldsymbol{\chi}) = \mathbb{A}^{\mathrm{el}}(\boldsymbol{\chi}) : \overline{\boldsymbol{\varepsilon}} \,. \tag{58}$$

The local strain concentration tensors in the RVE are fully characterized by the computation of local strains under certain different loading cases applied by prescribed strain boundary conditions $\overline{\boldsymbol{\varepsilon}}$ on the elastic RVE (Section 3.1). For the estimation of all local strain concentration tensors in a 3D heterogeneous structure, 6 different orthogonal boundary modes

$$\overline{\boldsymbol{\varepsilon}}^{(1)} = E\vec{e}_x \otimes \vec{e}_x \,, \tag{59a}$$
$$\overline{\boldsymbol{\varepsilon}}^{(2)} = E\vec{e}_y \otimes \vec{e}_y \,, \tag{59b}$$
$$\overline{\boldsymbol{\varepsilon}}^{(3)} = E\vec{e}_z \otimes \vec{e}_z \,, \tag{59c}$$
$$\overline{\boldsymbol{\varepsilon}}^{(4)} = \frac{1}{2}E(\vec{e}_x \otimes \vec{e}_y + \vec{e}_y \otimes \vec{e}_x) \,, \tag{59d}$$
$$\overline{\boldsymbol{\varepsilon}}^{(5)} = \frac{1}{2}E(\vec{e}_x \otimes \vec{e}_z + \vec{e}_z \otimes \vec{e}_x) \,, \tag{59e}$$
$$\overline{\boldsymbol{\varepsilon}}^{(6)} = \frac{1}{2}E(\vec{e}_y \otimes \vec{e}_z + \vec{e}_z \otimes \vec{e}_y) \tag{59f}$$

are applied on the RVE, with a strain magnitude E and the canonical unit vectors in a 3D space $\vec{e}_x$, $\vec{e}_y$ and $\vec{e}_z$. For 2D analyses, the boundary modes $\overline{\boldsymbol{\varepsilon}}^{(1)}$, $\overline{\boldsymbol{\varepsilon}}^{(2)}$ and $\overline{\boldsymbol{\varepsilon}}^{(4)}$ are applied. Writing Eq. (58) in Voigt-notation, the local elastic strain concentration tensors are fully characterized by a comparison of the resulting local strain field to the prescribed overall strain. After the determination of the full strain concentration tensor field, a k-means clustering technique (MacQueen (1967)) is applied on the local elastic strain concentration tensors. The k-means clustering approach divides the data points it is applied on, into a

number K of partitions by solving an optimization problem of the in-partition variances. Here, it is used as a multi-dimensional clustering approach, grouping all the fourth order strain concentration tensors at the microscopic points $\boldsymbol{\chi}$ inside one material phase V_Ω into a number of K_Ω partitions. During the clustering procedure, all tensor entries are taken into account, meaning that the dimensionality amounts to the number of (independent) components of a fourth-order tensor. The goal is the minimization of the function

$$H[\mathbb{A}^{\mathrm{el}}(\boldsymbol{\chi})] = \sum_{r=1}^{K_\Omega} \sum_{i=1}^{N_r} ||\mathbb{A}^{\mathrm{el}}(\boldsymbol{\chi}_i) - \mathbb{A}^{\mathrm{el}}_r||^2, \quad \boldsymbol{\chi} \in V_\Omega, \quad \boldsymbol{\chi}_i \in V_r \subset V_\Omega, \quad r \in 1, ..., K_\Omega \,, \tag{60}$$

where

$$||\mathbb{Z}|| = \sqrt{\mathbb{Z} :: \mathbb{Z}} \,, \tag{61}$$

indicated by optimal variances of the strain concentration tensors $\mathbb{A}^{\mathrm{el}}(\boldsymbol{\chi}_i)$ in one subdomain r to the corresponding subdomain average $\mathbb{A}^{\mathrm{el}}_r$ given by Eq. (56). The optimization problem is solved by an iterative process finally achieving the optimal decomposition of all data points into the K_Ω sets. This optimal decomposition of one material phase Ω is accomplished as follows:

1. First an arbitrary number of cluster K_Ω is chosen and strain concentration tensors at random data points are defined as the $r = 1, ..., K_\Omega$ initial cluster mean values $\mathbb{A}^{\mathrm{el}}_r$.

2. Iterative clustering procedure starts

   2.1. Variances of all local strain concentration tensors from the different cluster means

   $$||\mathbb{A}^{\mathrm{el}}(\boldsymbol{\chi}) - \mathbb{A}^{\mathrm{el}}_s||^2, \quad \boldsymbol{\chi} \in V_\Omega, \quad s \in 1, ..., K_\Omega \tag{62}$$

   are calculated. All corresponding local data points i are assigned to a set r, so that the variance between the local strain concentration tensor $\mathbb{A}^{\mathrm{el}}(\boldsymbol{\chi}_i)$ and the assigned cluster mean $\mathbb{A}^{\mathrm{el}}_r$ is minimal:

   $$||\mathbb{A}^{\mathrm{el}}(\boldsymbol{\chi}_i) - \mathbb{A}^{\mathrm{el}}_r||^2 \leq ||\mathbb{A}^{\mathrm{el}}(\boldsymbol{\chi}_i) - \mathbb{A}^{\mathrm{el}}_s||^2, \quad \begin{array}{l} \boldsymbol{\chi}_i \in V_r \subset V_\Omega, \\ \forall s,\, r \in 1, ..., K_\Omega,\, s \neq r \,. \end{array} \tag{63}$$

   2.2. Following, all strain concentration tensors assigned to the cluster are used to determine the updated cluster means $\mathbb{A}^{\mathrm{el}}_r$ using Eq. (56).

3. The iterative procedure ends when convergence of the procedure is reached, indicated by a stationary assignment of the local data points to the sets. The cluster means after convergence of the k-means clustering procedure act as the strain concentration tensors of the subdomains in the online stage.

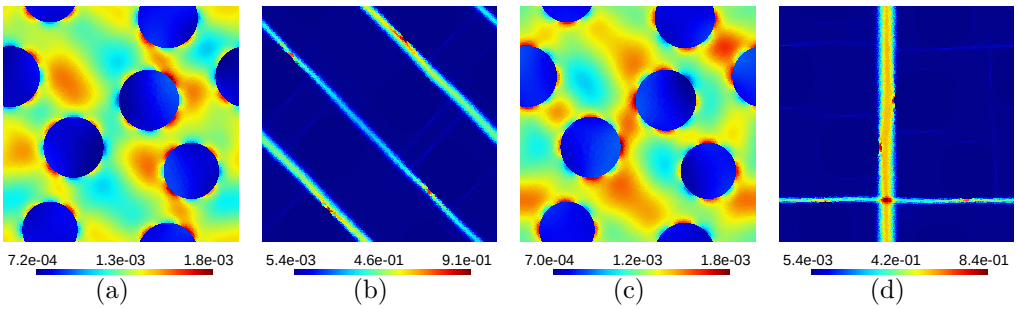

Figure 2: Computed equivalent strain fields following the application of the boundary condition states (a,b) bi-axial (as in Eq. (65a)) and (c,d) pure shear deformation (as in Eq. (65b)) during (a,c) purely elastic deformation and (b,d) after severe plastic deformation has occurred.

3.2.2. Subdomain decomposition based on local plastic fields

Inelastic deformation due to plastic flow, initiated when the initial yield limit of a material is exceeded, carries the major part of the total deformation in inelastic conditions. Inelastic deformation patterns in the material can deviate strongly from the spatial elastic deformation distributions (see Fig. 2), implying that subdivisions based on the distribution of elastic strain do not necessarily represent real deformation patterns during inelastic deformation. In this work, the eigenstrains introduced in Section 2 are equivalent to plastic strains as

$$\boldsymbol{\varepsilon}^{*} = \boldsymbol{\varepsilon}^{\mathrm{p}}. \tag{64}$$

In order to achieve an improved spatial division into subdomains for the modeling of inelastic processes, micromechanical deformation patterns occurring during inelastic deformation are captured by means of the conduction of simulations containing inelastic deformation in the material. For the investigated cases of 2D structures in this work, the following bi-axial and pure shear deformation boundary modes

$$\overline{\boldsymbol{\varepsilon}}^{\mathrm{in}(1)} = E^{\mathrm{in}}(\vec{e}_x \otimes \vec{e}_x - \vec{e}_y \otimes \vec{e}_y) \tag{65a}$$

$$\overline{\boldsymbol{\varepsilon}}^{\mathrm{in}(2)} = E^{\mathrm{in}}(\vec{e}_x \otimes \vec{e}_y + \vec{e}_y \otimes \vec{e}_x) \tag{65b}$$

with the overall deformation factor E^{in} were selected, both resulting in distinct isochoric deformation states and pure shearing in different orientations inside the material. The resulting inelastic deformation patterns are presented in Fig. 2.

After the choice of n_{p} (here $n_{\mathrm{p}} = 2$) different overall strain modes, the distinct simulations $l = 1, ..., n_{\mathrm{p}}$ with the corresponding boundary conditions $\overline{\boldsymbol{\varepsilon}}^{\mathrm{in}(l)}$ (Eq. (65)) are performed and the local plastic equivalent strain fields $\boldsymbol{\varepsilon}^{\mathrm{p}(l)}(\boldsymbol{\chi})$ computed. In order to capture plastic strain concentrations under different loading conditions more comparable, the computed plastic strain fields are normalized as

$$\boldsymbol{\phi}^{(l)}(\boldsymbol{\chi}) = \boldsymbol{\varepsilon}^{\mathrm{p}(l)}(\boldsymbol{\chi}) / p_{\Omega}^{(l)}, \quad \forall \boldsymbol{\chi} \in V_{\Omega}\,, \tag{66}$$

with the per-phase averaged equivalent plastic strain

$$p_\Omega^{(l)} = \sqrt{\frac{2}{3}\boldsymbol{\varepsilon}_\Omega^{\mathrm{p}^{(l)}} : \boldsymbol{\varepsilon}_\Omega^{\mathrm{p}^{(l)}}} \tag{67}$$

following from the plastic strain averaged over the corresponding material phase V_Ω

$$\boldsymbol{\varepsilon}_\Omega^{\mathrm{p}^{(l)}} = \frac{1}{|V_\Omega|}\int_{V_\Omega} \boldsymbol{\varepsilon}^{\mathrm{p}^{(l)}}(\boldsymbol{\chi})\mathrm{d}\boldsymbol{\chi}. \tag{68}$$

The Voigt notation is used for the transformation

$$\boldsymbol{\phi}^{(l)}(\boldsymbol{\chi}) \rightarrow \boldsymbol{q}^{(l)}(\boldsymbol{\chi}) \tag{69}$$

to obtain the local 6×1 vectors $\boldsymbol{q}^{(l)}(\boldsymbol{\chi})$[1]. Following, the normalized plastic strain fields are arranged in local $6\,n_\mathrm{P}$ vectors

$$\boldsymbol{q}(\boldsymbol{\chi}) = \left(\boldsymbol{q}^{(1)^T}(\boldsymbol{\chi}) \dots \boldsymbol{q}^{(n_\mathrm{p})^T}(\boldsymbol{\chi})\right)^\mathrm{T}, \tag{70}$$

representing the entirety of the local inelastic fields. A k-means clustering procedure similar to the one described above for the fourth-order elastic strain concentration tensors (Section 3.2.1) is performed, dividing all discrete material points in the considered RVE phase Ω into a number of K_Ω partitions r containing N_r data points based on the similarities of the local vectors $\boldsymbol{q}(\boldsymbol{\chi})$. The optimal decomposition is achieved by a minimization of the function

$$J[\boldsymbol{q}(\boldsymbol{\chi})] = \sum_{r=1}^{K_\Omega}\sum_{i=1}^{N_r} |\boldsymbol{q}(\boldsymbol{\chi}_i) - \boldsymbol{q}_r|^2, \quad \boldsymbol{\chi} \in V_\Omega, \quad \boldsymbol{\chi}_i \in V_r \subset V_\Omega, \quad r \in 1, ..., K_\Omega\,, \tag{71}$$

where

$$|\boldsymbol{z}| = \sqrt{\boldsymbol{z}\cdot\boldsymbol{z}}\,, \tag{72}$$

with the local vectors $\boldsymbol{q}(\boldsymbol{\chi}_i)$ inside the set r and the determined respective subdomain means $\boldsymbol{q}_r = \left(\boldsymbol{q}_r^{(1)} \dots \boldsymbol{q}_r^{(n_\mathrm{p})}\right)^\mathrm{T}$ following Eq. (56). After the division of all local points inside the microscopic RVE domain into subdomains based on inelastic fields, the strain concentration tensors $\mathbb{A}_r^\mathrm{el}$ of the subdomains r are determined using Eq. (56) following the application of the elastic loading modes (detailed in Section 3.2.1) given by Eq. (59).

3.2.3. Eigenstrain - strain interaction tensors between the subdomains

The TFA homogenization method relies on so-called interaction tensors, describing the elastic influences of eigenstrains at the "radiating" material points on the deformation field inside the RVE. The TFA relation under a vanishing overall strain is expressed following Eq. (14). Considering a uniform eigenstrain in one certain subdomain s as

$$\boldsymbol{\varepsilon}^*(\boldsymbol{\chi}') = \boldsymbol{\varepsilon}_s^*, \quad \boldsymbol{\chi}' \in V_s, \tag{73}$$

[1]Even for 2D cases, the 6 components of the plastic strain tensor are considered.

local strains are given as

$$\boldsymbol{\varepsilon}(\boldsymbol{\chi}) = \mathbb{D}_s(\boldsymbol{\chi}) : \boldsymbol{\varepsilon}_s^*, \tag{74}$$

with the local interaction function $\mathbb{D}_s(\boldsymbol{\chi})$ estimating the total effect of a uniform eigenstrain in an entire subdomain s on the strain at $\boldsymbol{\chi}$.

The eigenstrain-strain interaction tensors $\mathbb{D}_s(\boldsymbol{\chi})$ are determined by applying a vanishing overall strain, i.e. $\overline{\boldsymbol{\varepsilon}} = 0$, imposed by boundary conditions on the RVE in elasticity. Simultaneously, uniform eigenstrain modes are applied in each "radiating" subdomain s one at a time. The eigenstrain modes in 3D analyses are

$$\boldsymbol{\varepsilon}_s^{*(1)} = E^* \vec{e}_x \otimes \vec{e}_x \tag{75a}$$

$$\boldsymbol{\varepsilon}_s^{*(2)} = E^* \vec{e}_y \otimes \vec{e}_y \tag{75b}$$

$$\boldsymbol{\varepsilon}_s^{*(3)} = E^* \vec{e}_z \otimes \vec{e}_z \tag{75c}$$

$$\boldsymbol{\varepsilon}_s^{*(4)} = \frac{1}{2} E^* (\vec{e}_x \otimes \vec{e}_y + \vec{e}_y \otimes \vec{e}_x) \tag{75d}$$

$$\boldsymbol{\varepsilon}_s^{*(5)} = \frac{1}{2} E^* (\vec{e}_x \otimes \vec{e}_z + \vec{e}_z \otimes \vec{e}_x) \tag{75e}$$

$$\boldsymbol{\varepsilon}_s^{*(6)} = \frac{1}{2} E^* (\vec{e}_y \otimes \vec{e}_z + \vec{e}_z \otimes \vec{e}_y), \tag{75f}$$

while in 2D analyses, solely the modes $\boldsymbol{\varepsilon}_s^{*(1)}$, $\boldsymbol{\varepsilon}_s^{*(2)}$ and $\boldsymbol{\varepsilon}_s^{*(4)}$ are applied. The reaction strain field $\boldsymbol{\varepsilon}(\boldsymbol{\chi})$ emerging from the vanishing overall strain and each applied eigenstrain mode is computed. Local interaction tensors are fully characterized considering Eq. (74) in Voigt-notation and a comparison to the imposed eigenstrains in Eq. (75). Averaging the resulting strain field $\boldsymbol{\varepsilon}(\boldsymbol{\chi})$ over a certain subdomain V_r to achieve the subdomain strain

$$\boldsymbol{\varepsilon}_r = \frac{1}{|V_r|} \int_{V_r} \boldsymbol{\varepsilon}(\boldsymbol{\chi}) \, \mathrm{d}\boldsymbol{\chi} = \left[\frac{1}{|V_r|} \int_{V_r} \mathbb{D}_s(\boldsymbol{\chi}) \, \mathrm{d}\boldsymbol{\chi} \right] : \boldsymbol{\varepsilon}_s^* \tag{76}$$

leads to the characterization of the interaction tensors

$$\mathbb{D}_{rs} = \frac{1}{|V_r|} \int_{V_r} \mathbb{D}_s(\boldsymbol{\chi}) \, \mathrm{d}\boldsymbol{\chi} \tag{77}$$

between subdomains, such that

$$\boldsymbol{\varepsilon}_r = \mathbb{D}_{rs} : \boldsymbol{\varepsilon}_s^*. \tag{78}$$

In summary, the local fourth-order interaction tensors $\mathbb{D}_{rs}$ represent elastic influence factors of a uniform eigenstrain in the subdomain s on the average strain in the subdomain r.

3.3. Incorporation of a plastic correction based on real plastic field fluctuations

While the TFA used as a full-field modeling method as in Eq. (17) would lead to correct predictions of the materials behavior (Dvorak et al., 1994), it was recognized that, using the approximation of averages over subdomains, the tangent behavior of the material during inelastic deformation may be strongly over-estimated. This over-stiff modeled behavior

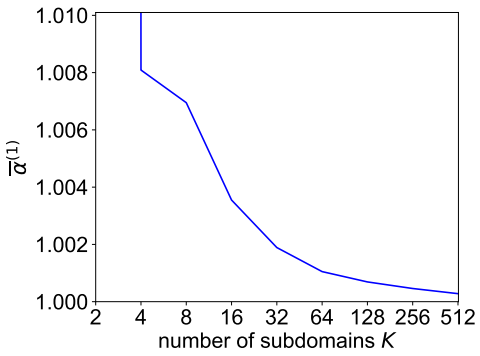

Figure 3: Exemplary computed total plastic fluctuation correction resulting from the application of the deformation mode $l = 1$ described in Eq. (65a) on the composite material with the volume fraction of inclusions $v_{\mathrm{II}} = 30$ % considered in Section 4.3.

is a consequence of under-estimated occurring plastic strain in plastically highly compliant material phases. Considering the numerical TFA approach, too low plastic strains imply under-estimated interaction effects between the phases and therefore inaccurate strain distributions over the phases, in particular under-estimated strains in plastic phases and therefore over-estimated strain accumulations in stiff phases. Over-estimated strain accumulations in stiff phases lead effectively to an over-stiff behavior of the overall composite material.

Chaboche et al. (2001) proposed an approach to artificially increase plastic strains in plastic subdomains by a consideration of a type of subdomains instantaneous strain concentration tensors. However, this approach has the following limitations: the used subdomains instantaneous strain concentration tensors are computed as the asymptotic strain concentration tensors, dependent solely on the known subdomains asymptotic tangent stiffness (not equivalent to the subdomain tangent stiffness in Eq. (52)). Firstly, the asymptotic tangent stiffness cannot be used for a non-linear hardening behavior, where the subdomains tangent stiffness is not constant. Secondly, the subdomains instantaneous strain concentration tensors can generally not be computed just from the local tangent stiffness. For an accurate estimation of the instantaneous strain concentration tensor, the overall tangent stiffness needs to be known as well (Dvorak (1992); Aboudi et al. (2013)).

In the following, it is accounted for a physical explanation of the over-stiff material behavior during inelastic deformation. The instantaneous spatial strain distribution in a material domain is constant as long as the material is deforming purely linear-elastic. This holds even if the material has experienced previous inelastic deformation. The stable strain distribution under elastic loads implies that it can be correctly recovered by means of the constant, once for all numerically determined, elastic strain concentration tensors. The constant strain distribution, however, does not hold for inelastic behavior of the material phases. Plastic strain is a direct consequence of the amount of local deformations during inelastic material behavior (Section 2.3). It means that high fluctuations in the localization of deformation are directly correlated to high plastic field fluctuations. Thus, plastic field fluctuations can be regarded as a marker for the heterogeneity of the local deformation field. In subdomains

with deformations considered as uniform, the microscopic yield starting points, and therefore the heterogeneity of the local onsets of non-linear behavior, are not well-represented. It implies that a certain degree of considered uniform, although actually heterogeneous, deformation $\boldsymbol{\varepsilon}_r$ of the subdomain leads to effectively under-estimated plastic yielding and thus plastic strains. This under-estimation worsens if the deformation accumulates in very localized zones, unable to be covered by the subdomains. Therefore, the more heterogeneous the actual deformation field in a subdomain, the higher becomes the under-estimation of the plastic strain due to the considered uniform deformation. The use of the TFA method using a finer decomposition into subdomains is motivated by a more accurate representation of the highly heterogeneous plastic field, resulting in a less stiff overall behavior of the material. If the spatial decomposition is the same as used in full-field simulations, the fluctuations are fully taken into account and the tangent behavior of the material can be estimated correctly (see the non-uniform TFA, Michel and Suquet (2003)).

In order to use the uniform TFA method and account for the problem of under-estimated inelastic and interaction effects in the subdomains due to the not well-captured deformation field heterogeneities, an artificial increase for the subdomains eigenstrain as in

$$\boldsymbol{\varepsilon}_r^{*^{\mathrm{corr}}} = p_r^{\mathrm{corr}} \boldsymbol{N}_r^{\mathrm{corr}} = f_r^{\mathrm{PFC}}\big(\boldsymbol{\varepsilon}_r^{\mathrm{p}}(\boldsymbol{\chi})\big)\, \boldsymbol{\varepsilon}_r^{*}. \tag{79}$$

is sought, with a plastic fluctuation correction (PFC) function f_r^{PFC} that depends on the magnitude of the fluctuations of the in-subdomain plastic field $\boldsymbol{\varepsilon}_r^{\mathrm{p}}(\boldsymbol{\chi})$. Since in case of a perfectly fine subdivision, and therefore no plastic fluctuations, the TFA leads to correct results, f_r^{PFC} must satisfy

$$\boldsymbol{\varepsilon}_r^{*^{\mathrm{corr}}} \to \boldsymbol{\varepsilon}_r^{*}, \quad \boldsymbol{\varepsilon}_r^{\mathrm{p}}(\boldsymbol{\chi}) \to \boldsymbol{\varepsilon}_r^{\mathrm{p}}\,, \quad \boldsymbol{\chi} \in V_r\,. \tag{80}$$

In this work, a first approach is tested, where f_r^{PFC} is considered as a scalar function $f_r^{\mathrm{PFC}} = \alpha_r$, correcting the subdomains equivalent plastic strain, while the plastic flow direction is not manipulated:

$$p_r^{\mathrm{corr}} = \alpha_r p_r\,, \quad \boldsymbol{N}_r^{\mathrm{corr}} = \boldsymbol{N}. \tag{81}$$

The particular proposed PFC factors in this paper are determined as the square root of the ratio between the arithmetic means $p_r^{(l)}$ and the harmonic means $\hat{p}_r^{(l)}$ of the plastic fields inside the subdomains. In the following, the procedure leading to the determination of the PFC correction for the subdomain r is described: After the RVE domain was subdivided into a certain number of subdomains based on the plastic fields $\boldsymbol{\varepsilon}^{\mathrm{p}^{(l)}}(\boldsymbol{\chi})$ under the loading modes $l = 1, ..., n_{\mathrm{p}}$, the before computed equivalent plastic strain field

$$p^{(l)}(\boldsymbol{\chi}) = \sqrt{\frac{2}{3}\boldsymbol{\varepsilon}^{\mathrm{p}^{(l)}}(\boldsymbol{\chi}) : \boldsymbol{\varepsilon}^{\mathrm{p}^{(l)}}(\boldsymbol{\chi})}\,. \tag{82}$$

is analyzed. Considering the equivalent plastic fields inside the subdomain r under each mode

$$p_r^{(l)}(\boldsymbol{\chi}) = p^{(l)}(\boldsymbol{\chi}), \quad \boldsymbol{\chi} \in V_r, \tag{83}$$

the arithmetic mean $p_r^{(l)}$ and the harmonic mean $\hat{p}_r^{(l)}$ are achieved using Eq. (56) and

$$\hat{p}_r^{(l)} = \left[\frac{1}{|V_r|} \int_{V_r} \frac{\mathrm{d}\boldsymbol{\chi}}{p^{(l)}(\boldsymbol{\chi})} \right]^{-1}. \tag{84}$$

Consequently, one PFC factor $\alpha_r^{(l)}$ for the subdomain r is determined under each of the n_p inelastic offline deformation modes l as a measure of the heterogeneity of the corresponding in-subdomain plastic fields $\boldsymbol{\varepsilon}_r^{\mathrm{p}^{(l)}}(\boldsymbol{\chi})$.

In cases of non-uniform distributions, the harmonic mean is always lower than the arithmetic mean. Since the harmonic mean is close to zero as soon as only a low number of material points exhibit no or very low plastic strains, a lower limit of plasticity inside the subdomain must be defined in order to achieve reasonable correction factors. Here, the PFC for a subdomain r is solely taken into account if $p_r^{(l)} \geq p_\Omega^{(l)}$, implying a sufficiently high harmonic mean of the plastic field. The formulation of the PFC finally reads

$$\alpha_r^{(l)} = \begin{cases} \sqrt{p_r^{(l)} / \hat{p}_r^{(l)}}\,, & p_r^{(l)} > p_\Omega^{(l)} \\ 1\,, \quad \text{otherwise.} \end{cases} \tag{85}$$

The expression Eq. (85) results in increasing corrections for the subdomains r the more the considered plastic field in the subdomain r varies. An increasing number of subdomains implies decreasing plastic field heterogeneities inside the subdomains and therefore decreasing correction effects as a function of the numbers of subdomains. The evolution of the total corrections $\bar{\alpha}^{(l)}$ (computed as in Eq. (55)) as a function of the used number of subdomains is presented in Fig. 3 for the exemplary case of the corrections $\alpha_r^{(1)}$ determined under the deformation mode $l = 1$. An additional restriction for the use of the PFC is mentioned: for reasons of an irregular behavior of the correction factors in the range of very low numbers of subdomains causing unreliable TFA modeling results, the PFC was not integrated for numbers of subdomains $K < 8$. For higher numbers of subdomains beyond the defined cut-off number of subdomains, i.e. for $K \geq 8$, a clear logarithmic decrease of the total correction $\bar{\alpha}_r^{(1)}$ (computed as in Eq. (55)) under an increasing number of subdomains is recognized. The selection of the correction factor α_r out of the pool $\alpha_r^{(1)}, ..., \alpha_r^{(n_\mathrm{p})}$ during the online stage is based on the current loading conditions, i.e. follows the consideration of the dominant component of the current overall strain increment $\Delta\overline{\boldsymbol{\varepsilon}}$:

$$\alpha_r = \begin{cases} \alpha_r^{(1)}\,, & \text{if } \Delta\overline{\boldsymbol{\varepsilon}}_{11} > \Delta\overline{\boldsymbol{\varepsilon}}_{12} \text{ or } \Delta\overline{\boldsymbol{\varepsilon}}_{22} > \Delta\overline{\boldsymbol{\varepsilon}}_{12} \\ \alpha_r^{(2)}\,, & \text{if } \Delta\overline{\boldsymbol{\varepsilon}}_{12} > \Delta\overline{\boldsymbol{\varepsilon}}_{11} \text{ and } \Delta\overline{\boldsymbol{\varepsilon}}_{12} > \Delta\overline{\boldsymbol{\varepsilon}}_{22}. \end{cases} \tag{86}$$

Therefore the correction factors can as well be applied for non-proportional loading histories $\overline{\boldsymbol{\varepsilon}}(t)$ containing different loading stages. If more different offline deformation modes were applied, the correction factor under the current loading could be selected based on minimal deviations between the various offline deformation modes $\overline{\boldsymbol{\varepsilon}}^{\mathrm{in}^{(l)}}$ and the current strain increment, i.e. $\alpha_r = \alpha_r^{(k)}$ if $||\Delta\overline{\boldsymbol{\varepsilon}} - \overline{\boldsymbol{\varepsilon}}^{\mathrm{in}^{(k)}}||^2 \leq ||\Delta\overline{\boldsymbol{\varepsilon}} - \overline{\boldsymbol{\varepsilon}}^{\mathrm{in}^{(m)}}||^2, \quad \forall m,\, k \neq m$ (where, in order to allow this comparison, all strain tensors should be normalized by their own equivalent

values). The proposed PFC in Eq. (79) with Eq. (81) modifies the original TFA constitutive equation Eq. (34) to

$$\Delta\boldsymbol{\varepsilon}_r = \mathbb{A}_r^{\mathrm{el}} : \Delta\overline{\boldsymbol{\varepsilon}} + \sum_{s=1}^{K} \alpha_s \mathbb{D}_{rs} : \Delta\boldsymbol{\varepsilon}_s^*. \tag{87}$$

Considering the property given in Eq. (32), which arises from the numerical evaluation of the tensors $\mathbb{D}_{rs}$ (Section 3.2.3), the modified condition for the interaction tensors

$$\sum_{r=1}^{K} \alpha_s \upsilon_r \mathbb{D}_{rs} = \alpha_s \left(\sum_{r=1}^{K} \upsilon_r \mathbb{D}_{rs} \right) = \mathbf{0}, \quad \forall s \in 1, ..., K \tag{88}$$

is automatically satisfied.

Algorithm 1: Numerical TFA procedure at a glance: Newton-Raphson scheme at one load step for a given overall strain increment $\Delta\overline{\boldsymbol{\varepsilon}}$.

initialize: $\Delta\boldsymbol{\varepsilon}_r = \mathbb{A}_r^{\mathrm{el}} : \Delta\overline{\boldsymbol{\varepsilon}}$ $(r = 1, ..., K)$
iterative procedure:
repeat
  for $r = 1, K$ **do**
    call constitutive relations for subdomain r to compute $\boldsymbol{\sigma}_r$, $\Delta\boldsymbol{\varepsilon}_r^*$ and $\partial\Delta\boldsymbol{\varepsilon}_r^*/\partial\boldsymbol{\varepsilon}_r$, $\mathbb{C}_r^{\tan}$ (details in Section 2.3)
  end
  for $r = 1, K$ **do**
    initialize residual $\boldsymbol{F}_r = \Delta\boldsymbol{\varepsilon}_r - \mathbb{A}_r^{\mathrm{el}} : \Delta\overline{\boldsymbol{\varepsilon}}$
    for $s = 1, K$ **do**
      add eigenstrain interaction contribution to residual:
      $\boldsymbol{F}_r = \boldsymbol{F}_r - \sum_s \alpha_s \mathbb{D}_{rs} : \Delta\boldsymbol{\varepsilon}_s^*$
      compute Jacobian matrix $\mathbb{J}_{rs} = \delta_{rs}\mathbb{I} - \alpha_s \mathbb{D}_{rs} : (\partial\Delta\boldsymbol{\varepsilon}_s^*/\partial\boldsymbol{\varepsilon}_s)$
    end
  end
  solve $\delta[\boldsymbol{\varepsilon}] = \{\mathbb{J}\}^{-1} : [\boldsymbol{F}]$
  update $[\Delta\boldsymbol{\varepsilon}] = [\Delta\boldsymbol{\varepsilon}] - \delta[\boldsymbol{\varepsilon}]$
until $|[\boldsymbol{F}]| < \mathrm{tol}$;
after convergence:
compute $\overline{\boldsymbol{\sigma}}$ and $\overline{\mathbb{C}}^{\tan}$, following Eq. (96) and Eq. (100), respectively.

3.4. Online stage: solution procedure using the TFA algorithm

In the following, the equations required to solve a mechanical problem using the TFA algorithm are derived. A schematic overview of the numerical TFA solution procedure is demonstrated in Algorithm 1.

The incremental TFA solution for the overall RVE response under a prescribed overall strain $\bar{\boldsymbol{\varepsilon}}$, is expressed as

$$\Delta\boldsymbol{\varepsilon}_r - \mathbb{A}_r^{\mathrm{el}} : \Delta\overline{\boldsymbol{\varepsilon}} - \sum_{s=1}^{K} \alpha_s \mathbb{D}_{rs} : \Delta\boldsymbol{\varepsilon}_s^* = 0\,, \tag{89}$$

where $\alpha_r = 1$ if the plastic fluctuation correction is not used. The numerical solution of this system is found using a Newton-Raphson procedure with the subdomain residuals

$$\boldsymbol{F}_r = \Delta\boldsymbol{\varepsilon}_r - \mathbb{A}_r^{\mathrm{el}} : \Delta\overline{\boldsymbol{\varepsilon}} - \sum_{s=1}^{K} \alpha_s \mathbb{D}_{rs} : \Delta\boldsymbol{\varepsilon}_s^*\,, \tag{90}$$

iteratively solving the problem $\boldsymbol{F}_r = 0$ by the linearization

$$\boldsymbol{F}_r \to \boldsymbol{F}_r + \delta\boldsymbol{F}_r = 0. \tag{91}$$

Expressed as an assembled system using the $K \times 1$ block column vectors denoted by "[ ]" and the square $K \times K$ block matrices denoted by "{ }", the variational term $\delta[\boldsymbol{F}]$ follows as

$$\delta[\boldsymbol{F}] = \left\{ \frac{\partial \boldsymbol{F}}{\partial \boldsymbol{\varepsilon}} \right\} : \delta[\boldsymbol{\varepsilon}] + \frac{\partial[\boldsymbol{F}]}{\partial \overline{\boldsymbol{\varepsilon}}} : \delta\overline{\boldsymbol{\varepsilon}} = \{\mathbb{J}\} : \delta[\boldsymbol{\varepsilon}] + \frac{\partial[\boldsymbol{F}]}{\partial \overline{\boldsymbol{\varepsilon}}} : \delta\overline{\boldsymbol{\varepsilon}}\,. \tag{92}$$

The full Jacobian system $\{\mathbb{J}\}$ consists of the single matrices (no sum on s intended)

$$\mathbb{J}_{rs} = \frac{\partial \boldsymbol{F}_r}{\partial \boldsymbol{\varepsilon}_s} = \delta_{rs}\mathbb{I} - \alpha_s \mathbb{D}_{rs} : \frac{\partial \Delta\boldsymbol{\varepsilon}_s^*}{\partial \boldsymbol{\varepsilon}_s}, \tag{93}$$

with the derivatives of the subdomain eigenstrains by the subdomain strains $\partial\Delta\boldsymbol{\varepsilon}_s^*/\partial\boldsymbol{\varepsilon}_s$ defined by Eq. (51). Assuming a constant homogenized strain, implying $\delta\overline{\boldsymbol{\varepsilon}} = 0$, the result

$$\delta[\boldsymbol{\varepsilon}] = -\{\mathbb{J}\}^{-1} : [\boldsymbol{F}] \tag{94}$$

is used to correct the strain increments in the subdomains by

$$[\boldsymbol{\varepsilon}] = [\boldsymbol{\varepsilon}] + \delta[\boldsymbol{\varepsilon}] \tag{95}$$

per iteration.

Once the computed strain increments of the subdomains have converged, the homogenized stress response is given by

$$\overline{\boldsymbol{\sigma}} = \sum_{r=1}^{K} v_r \boldsymbol{\sigma}_r\,. \tag{96}$$

The homogenized instantaneous stiffness is computed as

$$\overline{\mathbb{C}}^{\tan} = \frac{\partial \overline{\boldsymbol{\sigma}}}{\partial \overline{\boldsymbol{\varepsilon}}} = \sum_{r=1}^{K} v_r \frac{\partial \Delta\boldsymbol{\sigma}_r}{\partial \boldsymbol{\varepsilon}_r} \frac{\partial \boldsymbol{\varepsilon}_r}{\partial \overline{\boldsymbol{\varepsilon}}}\,, \tag{97}$$

where $\partial \Delta \boldsymbol{\sigma}_r / \partial \boldsymbol{\varepsilon}_r$ corresponds to the tangent operator of the subdomain (Eq. (52)). The second term

$$\frac{\partial \boldsymbol{\varepsilon}_r}{\partial \overline{\boldsymbol{\varepsilon}}} = \mathbb{A}_r^{\text{in}} \,, \tag{98}$$

representing the subdomains instantaneous strain concentration tensors $\mathbb{A}_r^{\text{in}}$, follows after the solution in Eq. (92) as

$$\frac{\partial [\boldsymbol{\varepsilon}]}{\partial \overline{\boldsymbol{\varepsilon}}} = -\{\mathbb{J}\}^{-1} : \frac{\partial [\boldsymbol{F}]}{\partial \Delta \overline{\boldsymbol{\varepsilon}}} = \{\mathbb{J}\}^{-1} : [\mathbb{A}^{\text{el}}] \,. \tag{99}$$

The resulting full expression of Eq. (97) amounts to

$$\overline{\mathbb{C}}^{\text{tan}} = \sum_{r=1}^{K} v_r \mathbb{C}_r^{\text{tan}} : \left[\sum_{s=1}^{K} \{\mathbb{J}\}_{rs}^{-1} : \mathbb{A}_s^{\text{el}} \right] = \sum_{r=1}^{K} v_r \mathbb{C}_r^{\text{tan}} : \mathbb{A}_r^{\text{in}} \,. \tag{100}$$

4. Numerical Applications

In this section, numerical applications of the TFA procedure described in this work are presented. Details of the offline (Section 4.1) and online (Section 4.2) stages, and the numerical results of applying the methods to different periodic two-phase structures with varying inclusion phase volume fractions, elastic and inelastic material properties and degrees of anisotropy are presented. The analysed material systems are

- a linear-elastic inclusion phase with isotropic elasticity in an elasto-plastic matrix phase in Section 4.3
- inclusions with higher and with lower elastic stiffness than the matrix phase and elasto-plastic behavior of both inclusion and matrix phases in Section 4.4
- a linear-elastic inclusion phase with transverse-isotropic elasticity in an elasto-plastic matrix phase for the case of elongated inclusions in Section 4.5. .

The material properties of the phases are denoted by the indices Ω = I, II, where the index I denotes the matrix and the index II the inclusion phase.

4.1. Offline stage

Cluster decompositions are consequences of the two different clustering techniques described in Section 3.2.1 based on elastic and in Section 3.2.2 based on plastic strain distributions.

Practical information for the conduction of the offline stage simulations under inelastic conditions are presented. While the elastic phase properties used during the offline stage must be equal to the ones considered in the online stage, the inelastic properties are allowed to differ. The purpose of the choice of the inelastic phase properties during the offline stage is the ability to identify the inelastic deformation patterns in order to achieve well-represented inelastic fields by the spatial division. In the following, the superscript "off" for the material

properties denotes that these values are used in the offline stage and are not necessarily the same as the material properties considered in the online stage. In case of elastic inclusions in an elasto-plastic matrix phase, the low yield strength $\sigma_{\mathrm{I}}^{\mathrm{Y0,off}} = 10$ MPa and the inelastic behavior given by the power-law hardening relation

$$R = H_{\mathrm{I}}^{\mathrm{off}}\, p^{m_{\mathrm{I}}^{\mathrm{off}}} \tag{101}$$

with the hardening modulus $H_{\mathrm{I}}^{\mathrm{off}} = 50$ MPa and hardening exponent $m_{\mathrm{I}}^{\mathrm{off}} = 0.05$ are used in the offline stage, causing high plastic localizations, which enables the identification of localized deformations. A convergence study was performed in order to specify the overall deformation factor E^{in} that determines the degree of the RVE deformation (Section Appendix B). It was found that, using the aforementioned inelastic material properties, the final plastic field patterns are established under an overall deformation of 2 %. Therefore, the overall deformation factor $E^{\mathrm{in}} = 2$ % was chosen for the offline deformation modes. In the case of elasto-plasticity in both phases, low yield strengths values $\sigma_{\mathrm{I}}^{\mathrm{Y0,off}} = \sigma_{\mathrm{II}}^{\mathrm{Y0}} = 10$ MPa are used and the inelastic behavior in each phase is expressed by the power-law relation

$$R = H_{\Omega}^{\mathrm{off}}\, p^{m_{\Omega}^{\mathrm{off}}}, \quad \Omega = \mathrm{I,II} \tag{102}$$

with $m_{\Omega}^{\mathrm{off}} = 0.05$. In case of an inclusion phase that is stiffer than the matrix phase, the hardening moduli are $H_{\mathrm{I}}^{\mathrm{off}} = 50$ MPa and $H_{\mathrm{II}}^{\mathrm{off}} = 100$ MPa. In the reversed case of a more compliant inclusion phase, the hardening moduli $H_{\mathrm{II}}^{\mathrm{off}} = 50$ MPa and $H_{\mathrm{I}}^{\mathrm{off}} = 100$ MPa are reversed.

4.2. Online tests

Subsequently, different numerical tests were performed, described by the following boundary conditions:

- prescribed overall axial loading-unloading cycle up to 6% strain in x-axis orientation with free motion of one edge with its normal in y-orientation, corresponding to overall uni-axial tension boundary conditions

$$\begin{aligned} &\overline{\varepsilon}_{xx} = 0 \rightarrow 0.06 \rightarrow 0 \\ &\overline{\sigma}_{yy} = 0,\ \overline{\varepsilon}_{zz} = 0\,; \end{aligned} \tag{103}$$

- prescribed overall pure shear strain loading-unloading cycle up to 4%

$$\overline{\boldsymbol{\varepsilon}} = \begin{pmatrix} 0 & 0 \\ 0 & 0 \end{pmatrix} \rightarrow \begin{pmatrix} 0 & 0.04 \\ 0.04 & 0 \end{pmatrix} \rightarrow \begin{pmatrix} 0 & 0 \\ 0 & 0 \end{pmatrix}; \tag{104}$$

- non-proportional prescribed loading consisting of four different stages of bi-axial isochoric and shear loading and unloading stages, represented by the overall strain evolution $\overline{\boldsymbol{\varepsilon}}(t)$, with $\overline{\varepsilon}_{zz} = 0$:

$$\begin{aligned} \overline{\boldsymbol{\varepsilon}}(0) = \begin{pmatrix} 0 & 0 \\ 0 & 0 \end{pmatrix} \rightarrow \overline{\boldsymbol{\varepsilon}}(T/4) = \begin{pmatrix} 0.06 & 0 \\ 0 & -0.06 \end{pmatrix} \rightarrow \overline{\boldsymbol{\varepsilon}}(T/2) = \begin{pmatrix} 0.06 & 0.04 \\ 0.04 & -0.06 \end{pmatrix} \\ \rightarrow \overline{\boldsymbol{\varepsilon}}(3T/4) = \begin{pmatrix} 0 & 0.04 \\ 0.04 & 0 \end{pmatrix} \rightarrow \overline{\boldsymbol{\varepsilon}}(T) = \begin{pmatrix} 0 & 0 \\ 0 & 0 \end{pmatrix}. \end{aligned} \tag{105}$$

The resulting homogenized axial stress-strain responses under the uni-axial tension and shear stress-strain responses under the pure shearing conditions computed by the TFA algorithm (Section 3.4) based on the underlying foundations for the subdomain decomposition are presented. Displayed are computed stress-strain responses by the TFA and the FE method, and a convergence analysis based on the peak stresses computed by the TFA tending towards the peak stresses computed by the FE method when increasing the number of subdomains. The deviations of the homogenized axial and shear peak stresses $\max(\overline{\boldsymbol{\sigma}})^{\mathrm{TFA}}_{xx}$, $\max(\overline{\boldsymbol{\sigma}})^{\mathrm{TFA}}_{xy}$ by the TFA to the corresponding peak stresses $\max(\overline{\boldsymbol{\sigma}})^{\mathrm{FE}}_{xx}$, $\max(\overline{\boldsymbol{\sigma}})^{\mathrm{FE}}_{xy}$ computed by the FE method under uni-axial tension and pure shearing, respectively, lead to the TFA error estimations

$$e_{xx} = \left[\frac{\max(\overline{\boldsymbol{\sigma}}_{xx})^{\mathrm{TFA}} - \max(\overline{\boldsymbol{\sigma}}_{xx})^{\mathrm{FE}}}{\max(\overline{\boldsymbol{\sigma}}_{xx})^{\mathrm{FE}}}\right] \times 100\% \,, \tag{106a}$$

$$e_{xy} = \left[\frac{\max(\overline{\boldsymbol{\sigma}}_{xy})^{\mathrm{TFA}} - \max(\overline{\boldsymbol{\sigma}}_{xy})^{\mathrm{FE}}}{\max(\overline{\boldsymbol{\sigma}}_{xy})^{\mathrm{FE}}}\right] \times 100\% \,. \tag{106b}$$

In the following, the TFA with one subdomain per material phase, equivalent to a mean-field approach, is referred to as TFA-MF, the TFA with a subdomain decomposition based on elasticity is referred to as TFA-E. The new approach using a plasticity-based foundation for the spatial decomposition is referred to as TFA-P. The use of the plastic fluctuation correction for the TFA-P (as described in Section 3.3) is referred to as TFA-PFC.

4.3. Isotropic microstructures with elastic inclusions

Considered is an isotropic microstructure, which consists of a matrix material with circular inclusions covering a volume fraction of successively $\upsilon_{\mathrm{II}} = 20$ %, 30 % and 50 % (see Fig. 4). The elastic properties of the two phases are given in terms of the following bulk and shear moduli

- matrix: bulk modulus $\kappa_{\mathrm{I}} = 10$ GPa and shear modulus $\mu_{\mathrm{I}} = 3$ GPa;
- inclusion phase: bulk modulus $\kappa_{\mathrm{II}} = r_{\mathrm{II}}\kappa_{\mathrm{I}}$ and shear modulus $\mu_{\mathrm{II}} = r_{\mathrm{II}}\mu_{\mathrm{I}}$, with successive values of r_{II} =2, 10 and 100.

4.3.1. Spatial division into subdomains

The offline stage simulations were performed using a mesh consisting of 26508 and 27656 quadratic triangular elements for respectively $\upsilon_{\mathrm{II}} = 20$ % and υ_{II} =30 %. For the RVE with the volume fraction of inclusions υ_{II} =50 %, the effect of a mesh refinement is studied by considering two meshes of 40278 and 158420 triangular quadratic elements. Considered is a material system consisting of an elasto-plastic matrix material reinforced by stiff linear-elastic inclusions. The material properties used for the inelastic conditions in the offline stage for this material system are given in Section 4.1. Under both deformation modes, the inelastic deformation is carried by a low number of plastic shear bands, traversing the material through the inter-inclusion spaces. While under the bi-axial isochoric deformation mode, the plastic shear bands crossing the material are diagonally oriented, the pure shear

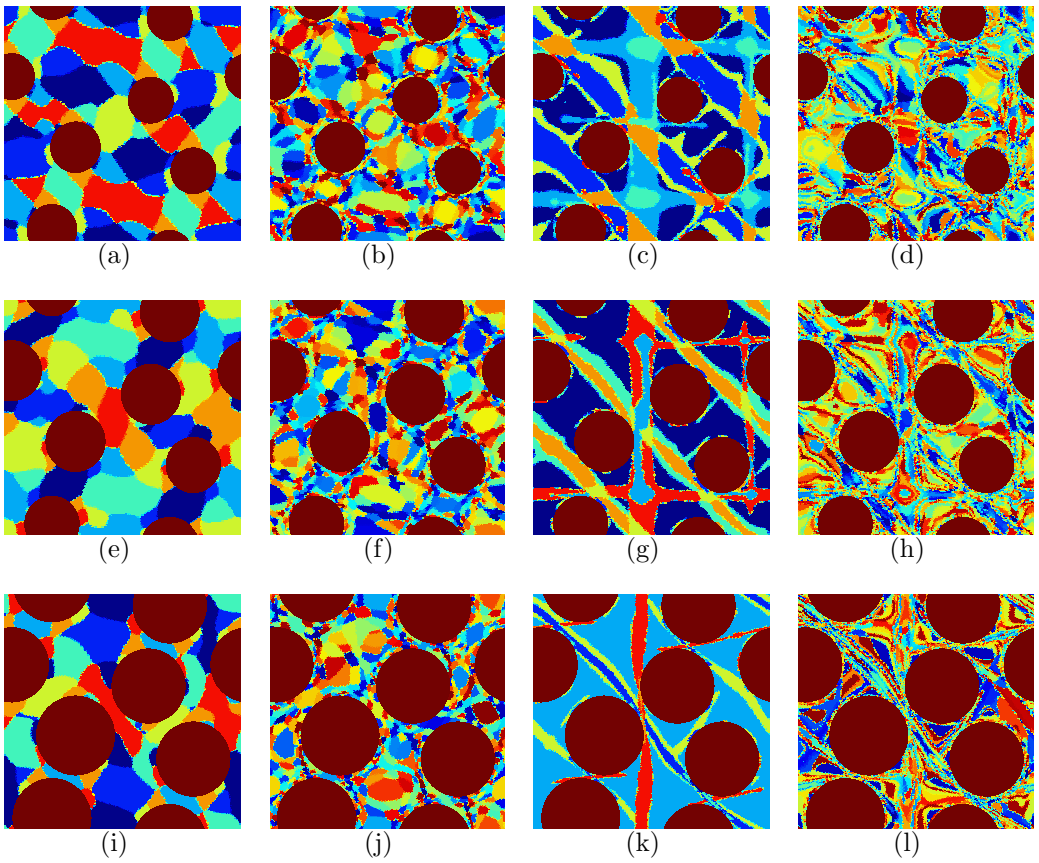

Figure 4: Microstructure of the composite materials with (a-d) $v_{\mathrm{II}} = 20$ % , (e-h) $v_{\mathrm{II}} = 30$ % and (i-l) $v_{\mathrm{II}} = 50$ % circular stiff elastic inclusions in an elasto-plastic matrix (case of 40278 elements), and spatial decompositions based on elastic deformation into (a, e, i) 8 subdomains and (c, g, k) 128 subdomains and based on inelastic deformation into (b, f, j) 8 subdomains and (d, h, l) 128 subdomains.

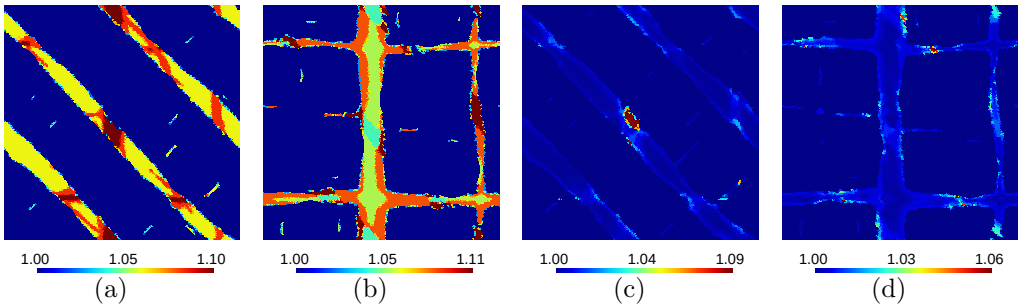

Figure 5: Spatial distribution of the plastic fluctuation corrections (PFC) $\alpha_r^{(1)}$ (a, c) and $\alpha_r^{(2)}$ (b, d) for the microstructure with $v_{\mathrm{II}} = 30$ % elastic inclusions for the cases of 8 (a, b) and 128 (c, d) subdomains.

Table 1: Peak stress errors (computed as in Eq. (106)) using the different TFA approaches for the composite material with different volume fractions v_{II} of circular stiff elastic inclusions embedded in a perfectly plastic matrix (Fig. 4).

v_{II} =20%	TFA-E 512	TFA-P 512	TFA-PFC 512
e_{xx} (%)	9	5	4
e_{xy} (%)	8	2	2
v_{II} =30%	TFA-E 512	TFA-P 512	TFA-PFC 512
e_{xx} (%)	19	8	7
e_{xy} (%)	15	5	4
v_{II} =50%	TFA-E 512	TFA-P 512 (coarse/fine)	TFA-PFC 512 (coarse/fine)
e_{xx} (%)	51	42/36	36/30
e_{xy} (%)	41	27/19	17/11

deformation mode causes plastic shear bands in axial orientations. Solely the thickness of the band-like structures changes in dependence of the inclusion phase volume fraction: In case of the lower volume fraction and higher inter-inclusion spaces, the plastic bands are wider, while in case of the high volume fraction and therefore narrow inter-inclusion spaces, the plastic bands are narrower. The full-field RVE domain was divided in the offline stage into K = 2, 16, 32, 64, 128, 256, 512 subdomains, of which one subdomain is sufficient to represent the elastic inclusion phase. The spatial subdivisions of the RVE into K = 8 and K = 128 subdomains based on elastic and based on plastic deformation are displayed in Fig. 4 (for the case of v_{II} =50 %, only the decomposition for the mesh of 40278 triangular quadratic elements is shown). The consideration of plastic strain distributions allows a spatial subdivision representing the inelastic band-like deformation patterns and their intersections. The Fig. 5 shows the spatial distribution of the PFC factors (Section 3.3), representing the degree of the plastic heterogeneity in the subdomains, after the inelasticity-based clustering of the RVE domain with v_{II} =30 into 8 and 128 subdomains (see Figs. 4(g) and 4(h)). The highest values (red color) of the PFC are located in regions with high plastic strain concentrations, being not sufficiently captured by the clustering, what leads to high local plastic field fluctuations inside the subdomains. This occurs for example in regions where the plastic deformation patterns under the different offline deformation cases intersect (see the dark red regions in Figs. 5(a) and 5(b)). In these regions, the clustering needs to account for the inelastic fields under both deformation modes, leading to a less accurate coverage of the single inelastic fields. Furthermore, the decrease of the PFC factor values with an increasing number of subdomains (see Eq. (80)) is clearly visible.

4.3.2. Effect of the volume fraction of the inclusion phase

The matrix material behaves perfectly plastic with the yield strength $\sigma_{\mathrm{I}}^{\mathrm{Y0}} = 100$ MPa, while the inclusions deform linearly-elastic. The elastic stiffness contrast between both phases is taken as r_{II} =2. For both tested loading cases of uni-axial tension and pure shear deformation, the stress-strain responses of the composite material are displayed in Figs. 6-8

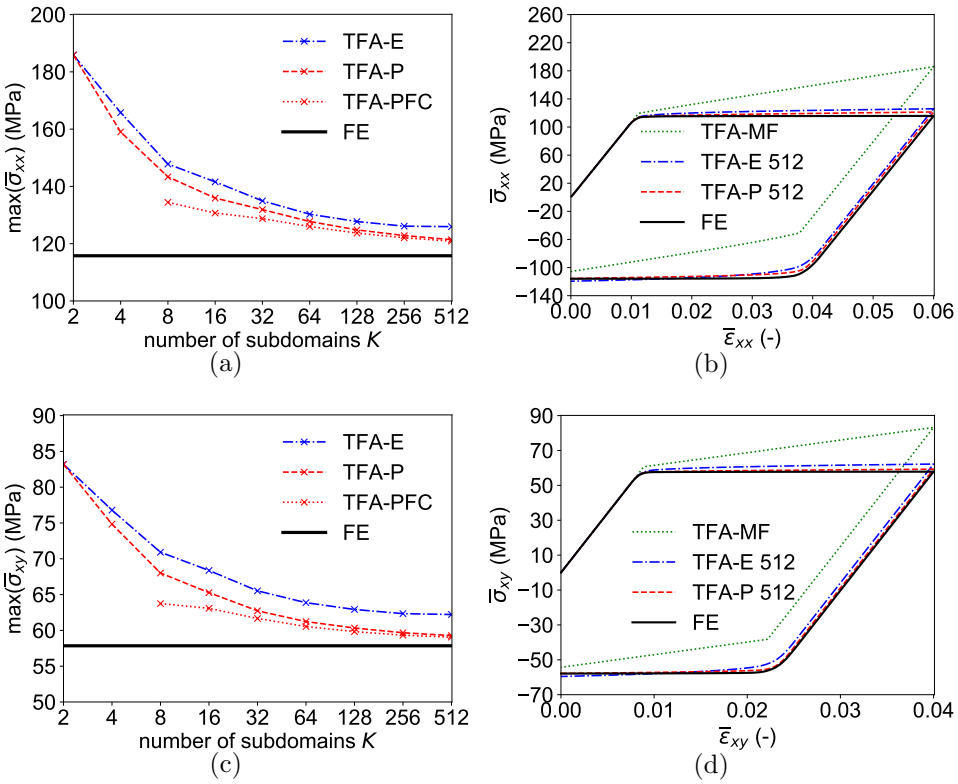

Figure 6: Normal stress response under uni-axial tension (Eq. (103)) and shear stress response under pure shear deformation (Eq. (104)) of a composite material with $v_{\mathrm{II}} = 20$ % of circular stiff elastic inclusions embedded in a perfectly plastic matrix in comparison to the full-field FE result. Displayed are (a, c) the convergence of the peak stress depending on the number of subdomains (Fig. 4) and (b, d) stress-strain curves computed by the different TFA approaches.

for the three tested volume fractions, and the peak stress errors at maximum loading are reported in Table 1.

For low and moderate volume fractions, it is visible in Figs. 6(a) and 6(c) and in Figs. 7(a) and 7(c) that the TFA-P allows a better convergence towards the reference result than the TFA-E throughout the whole range of the numbers of subdomains, and continues to converge in the region of high numbers of subdomains $K \geq 256$, where the TFA-E results do not significantly improve anymore. Consequently, the peak stress errors can be strongly reduced using the TFA-P in comparison with the TFA-E, while the TFA-PFC provides an additional improvement that decreases with increasing numbers of subdomains. The stress-strain responses computed by the TFA-P and TFA-PFC with 512 subdomains cover the reference stress-strain responses computed by the full-field homogenization closely and with significantly higher accuracy than the TFA-E (Figs. 6(b) and 6(d) and Figs. 7(b) and 7(d)).

Considering the higher inclusion volume fraction in Figs. 8(a) and 8(c), the TFA-E achieves better results than the TFA-P in the range of low numbers of subdomains. However, the convergence rate of the TFA-E method starts to decrease earlier then the conver-

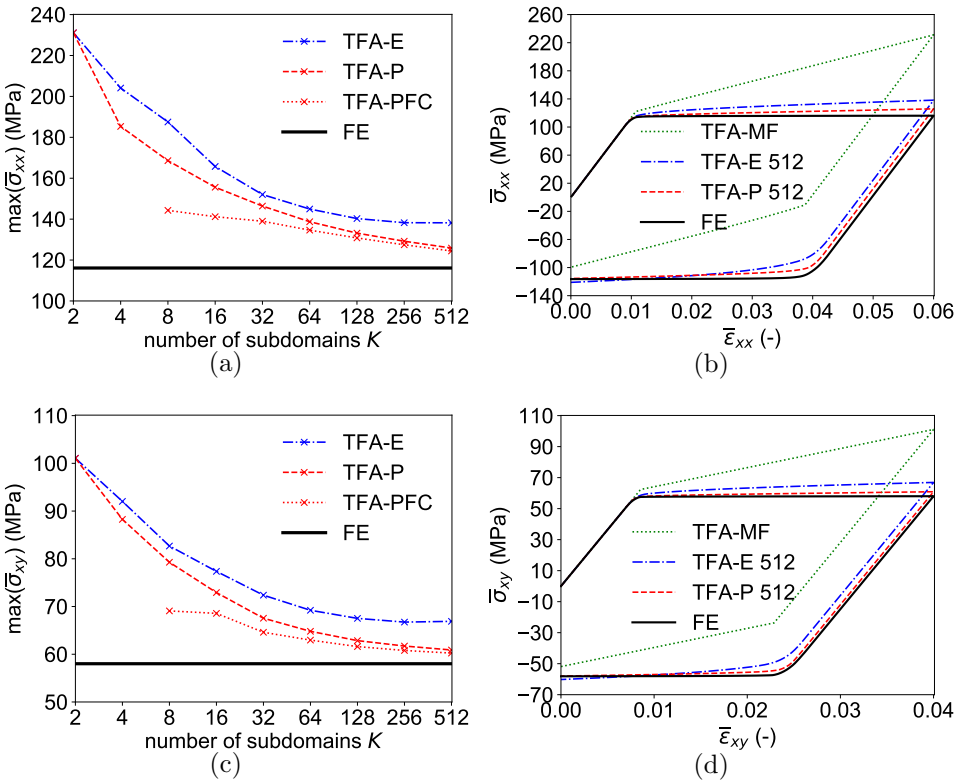

Figure 7: Normal stress response under uni-axial tension (Eq. (103)) and shear stress response under pure shear deformation (Eq. (104)) of a composite material with $v_{\mathrm{II}} = 30$ % of circular stiff elastic inclusions embedded in a perfectly plastic matrix in comparison to the full-field FE result. Displayed are (a, c) the convergence of the peak stress depending on the number of subdomains (Fig. 4(e-h)) and (b, d) stress-strain curves computed by the different TFA approaches.

gence rate of the TFA-P, leading to better TFA-P results in the range of high numbers of subdomains. Nonetheless, clearly stiffer stress-strain responses than for the lower volume fractions are achieved using the TFA-E and TFA-P approaches with up to 512 subdomains (Figs. 8(b) and 8(d)). Furthermore it is visible that the TFA-P prediction does not continue to converge towards the reference results in the range $256 \leq K \leq 512$ when the spatial division is based on offline simulations using the coarse mesh. The fading convergence implies that the k-means clustering was not able to define a meaningful subdomain refinement for $K > 256$. For this reason, the previously mentioned refined mesh, with half dimensions for the triangular quadratic elements, was tested in the offline stage for comparison. It is recognized that the use of a finer mesh allows further improvements of accuracy and a proceeding convergence towards the full-field results (denoted as TFA-P fine in Figs. 8(a) and 8(c)). The TFA-PFC provides a slight improvement for the uni-axial tension test and a significant error reduction for the pure shear test (Table 1). Mentioned are the fluctuations in the TFA results in the range of low numbers of subdomains up to $K \leq 32$ due to an irregular behavior of the correction factor (see Section 3.3).

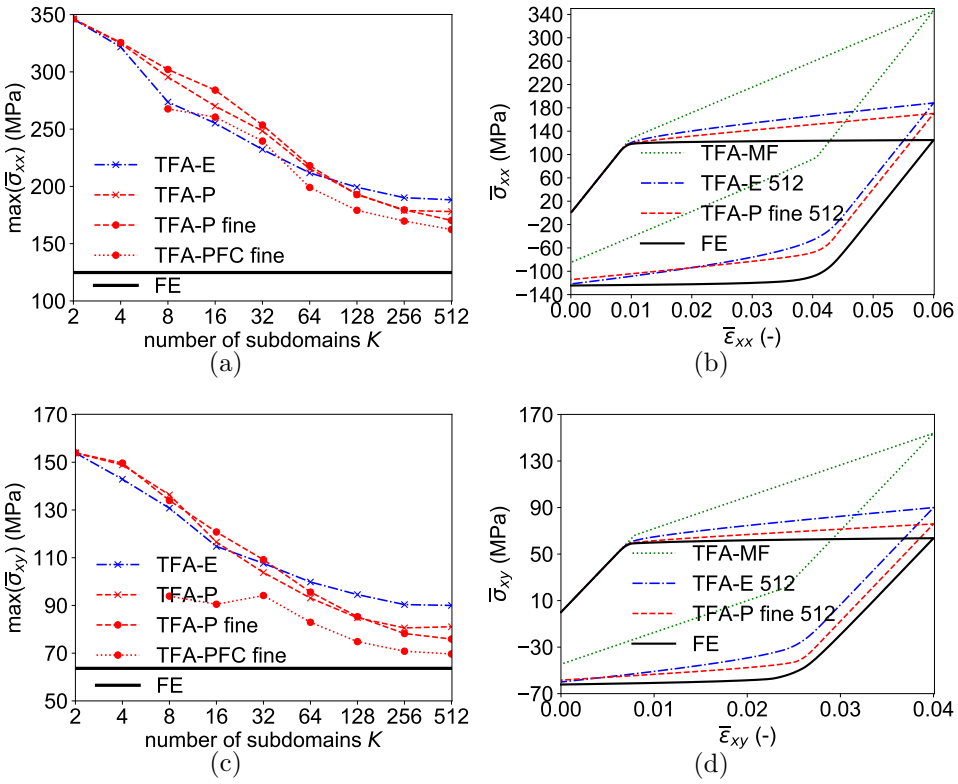

Figure 8: Normal stress response under uni-axial tension (Eq. (103)) and shear stress response under pure shear deformation (Eq. (104)) of a composite material with $v_{\mathrm{II}} = 50$ % of circular stiff elastic inclusions embedded in a perfectly plastic matrix in comparison to the full-field FE result. Displayed are (a, c) the convergence of the peak stress depending on the number of subdomains (Fig. 4(i-l)) and (b, d) stress-strain curves computed by the different TFA approaches.

4.3.3. Effect of the elastic stiffness contrast between the phases

The RVE with the inclusion volume fraction $v_{\mathrm{II}} = 30\%$ is considered, now with an increased elastic stiffness of the inclusion phase. The elastic properties of the matrix remain the same as before and it follows a perfectly plastic behavior. While in the examples above (Section 4.3.2), the ratio of the Young's moduli of the inclusion phase and the matrix phase was $r_{\mathrm{II}} = 2$, this ratio is increased to $r_{\mathrm{II}} = 10$ and $r_{\mathrm{II}} = 100$. Since it was recognized that the TFA yields over-stiff results due to overestimated deformations of stiff elastic phases, the investigation of high elastic stiffness contrasts is an important test of the TFA abilities for general composite materials. With the same RVE and material system of elastic inclusions in an elasto-plastic matrix as in the first example of this section and consequently the same inelastic patterns, the subdomain decompositions are nearly identical to the ones in Fig. 4(e-h), and therefore not displayed. Throughout the whole range of numbers of subdomains, the TFA-P leads to improved results compared to the TFA-E, with the TFA-PFC allowing for further improvements of accuracy in both the uni-axial tension and pure shear tests in the region of low and intermediate numbers of subdomains $8 \leq K \leq 128$. (Figs. 9 and 10).

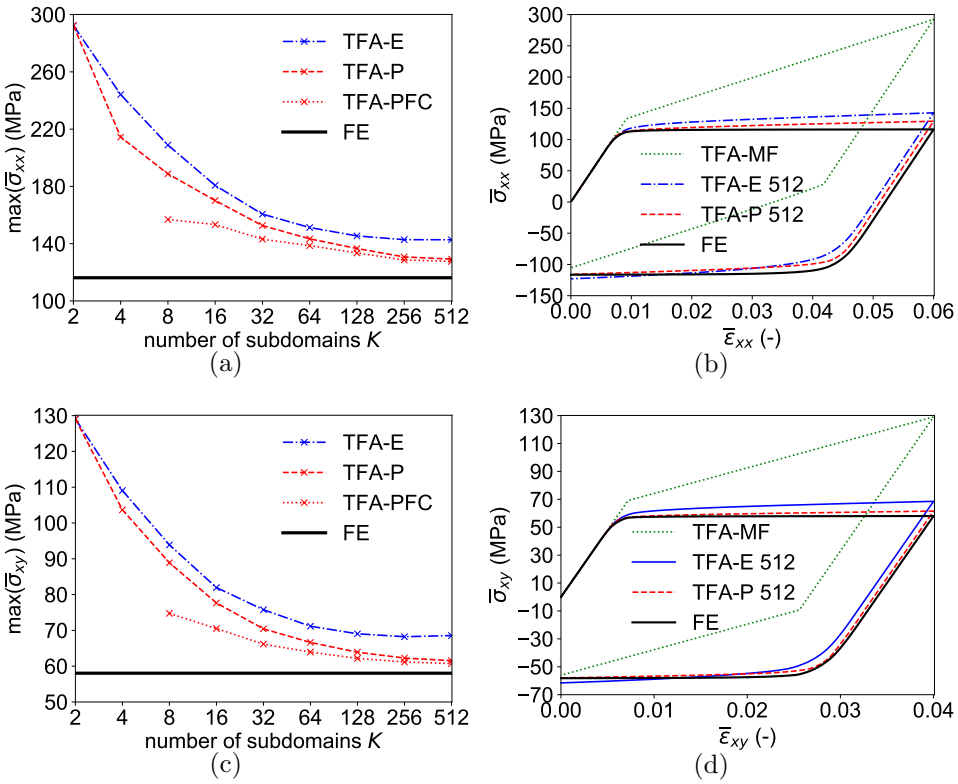

Figure 9: Normal stress response under uni-axial tension (Eq. (103)) and shear stress response under pure shear deformation (Eq. (104)) of a composite material with $v_{\mathrm{II}} = 30$ % (Fig. 4(e-h)) consisting of circular stiff elastic inclusions embedded in a perfectly plastic matrix with a ratio of the Young's moduli $r_{\mathrm{II}} = 10$ in comparison to the full-field FE result. Displayed are (a,c) the convergence of the peak stress depending on the number of subdomains and (b,d) stress-strain curves computed by the different TFA approaches.

Table 2: Peak stress errors (computed as in Eq. (106)) using the different TFA approaches for the composite material with $v_{\mathrm{II}} = 30$ % (Fig. 4(e-h)) consisting of circular stiff elastic inclusions embedded in a perfectly plastic matrix for different phases Young's moduli ratios r_{II}.

$r_{\mathrm{II}} = 2$	TFA-E 512	TFA-P 512	TFA-PFC 512
e_{xx} (%)	19	8	7
e_{xy} (%)	15	5	4
$r_{\mathrm{II}} = 10$	TFA-E 512	TFA-P 512	TFA-PFC 512
e_{xx} (%)	23	11	9
e_{xy} (%)	18	6	5
$r_{\mathrm{II}} = 100$	TFA-E 512	TFA-P 512	TFA-PFC 512
e_{xx} (%)	24	11	9
e_{xy} (%)	19	6	4

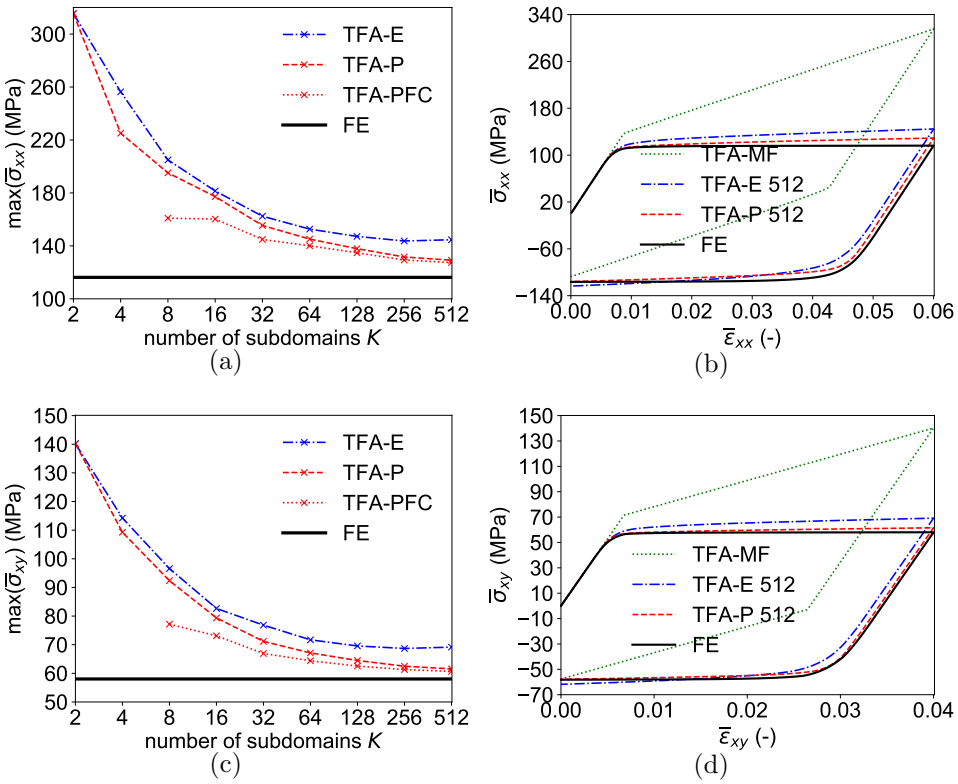

Figure 10: Normal stress response under uni-axial tension (Eq. (103)) and shear stress response under pure shear deformation (Eq. (104)) of a composite material with $v_{\mathrm{II}} = 30$ % (Fig. 4(e-h)) consisting of circular stiff elastic inclusions embedded in a perfectly plastic matrix with a ratio of the Young's moduli $r_{\mathrm{II}} = 100$ in comparison to the full-field FE result. Displayed are (a,c) the convergence of the peak stress depending on the number of subdomains and (b,d) stress-strain curves computed by the different TFA approaches.

A comparison of the initial case $r_{\mathrm{II}} = 2$ and the two cases $r_{\mathrm{II}} = 10$ and $r_{\mathrm{II}} = 100$ shows a decreasing TFA-E accuracy with increasing stiffness of the inclusion phase. In opposition to that, the TFA-P is only weakly affected by the increasing inclusion stiffness and provides accurate results with 512 subdomains (Table 2). The TFA-PFC nearly recovers the reference results with hardly rising errors due to the increasing inclusion phase stiffness.

4.3.4. Effect of the RVE size

Table 3: Peak stress errors (computed as in Eq. (106)) using the different TFA approaches for the larger composite RVE with $v_{\mathrm{II}} = 50$ % (Fig. 11) consisting of circular stiff elastic inclusions embedded in a perfectly plastic matrix.

$v_{\mathrm{II}} = 50$ %	TFA-E 512	TFA-P 512	TFA-PFC 512
e_{xx} (%)	57	37	30
e_{xy} (%)	37	16	10

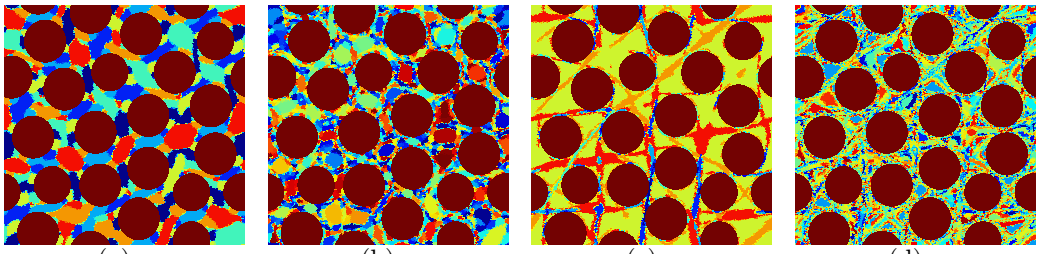

(a) (b) (c) (d)

Figure 11: Microstructure and spatial decompositions of the larger composite RVE with $v_{\mathrm{II}} = 50$ % of circular stiff elastic inclusions in an elasto-plastic matrix based on elastic deformation into (a) 8 subdomains and (b) 128 subdomains and based on inelastic deformation into (c) 8 subdomains and (d) 128 subdomains.

In the examples above, relatively small extracts of microstructures were considered as RVEs. In this section, the TFA is applied for the case of a real representative portion of an isotropic microstructure with an inclusions volume fraction $v_{\mathrm{II}} = 50\%$, expected to contain higher varieties of deformation states within the RVE. By this application it is investigated if equal degrees of accuracy as for smaller RVEs are achieved for a real RVE using the same range of numbers of subdomains. The elastic (the phase contrast $r_{\mathrm{II}} = 2$ is considered for this application) and inelastic phase properties are the same as in Section 4.3.2. The offline stage simulations were performed with a mesh consisting of 40460 triangular quadratic elements, which corresponds to the coarse mesh size for the small RVE with $v_{\mathrm{II}} = 50\%$ in Section 4.3.2. The inelastic deformation again localizes in plastic shear band deformation patterns, oriented diagonally resulting from bi-axial isochoric and oriented axially resulting from the pure shear deformation mode. In comparison to the examples above, the number of band-like structures is increased, with some of them still traversing the whole material domain in the presence of a much higher number of obstacles. Following, the RVE domain was divided into $K = 2$, 16, 32, 64, 128, 256, 512 subdomains. The microstructure and the spatial divisions resulting from elastic and inelastic deformation into 8 and 128 subdomains are displayed in Fig. 11.

The results of convergence analyses are presented in Fig. 12. The TFA-E and the TFA-P have an equal rate of convergence towards the full-field result in the range $K \leq 32$ in the uni-axial tension test. After this point, the TFA-P shows a faster decrease in error than the TFA-E and therefore allows improved stress-strain predictions (Figs. 12(a) and 12(b)). The error by the TFA-P with 512 subdomains is still considerably high but significantly lower than the one by the TFA-E, and the TFA-PFC provides complementary improvements (Table 3). Furthermore, the convergence of the transverse strain $\overline{\boldsymbol{\varepsilon}}_{yy}$ and the evolution of the homogenized Poisson ratio $\overline{\nu}_{xy}(\overline{\boldsymbol{\varepsilon}}_{xx})$ using the TFA-P and TFA-PFC methods during the uni-axial tension test were investigated and are presented in Figs. 12(c) and 12(d). Similarly to the stress response, the TFA-P and TFA-PFC allow a better convergence of $\overline{\boldsymbol{\varepsilon}}_{yy}$ than the TFA-E towards the FE result. The TFA-PFC allows for slightly better estimations of the instantaneous Poisson ratio than the TFA-P. Considering the the pure shear test,

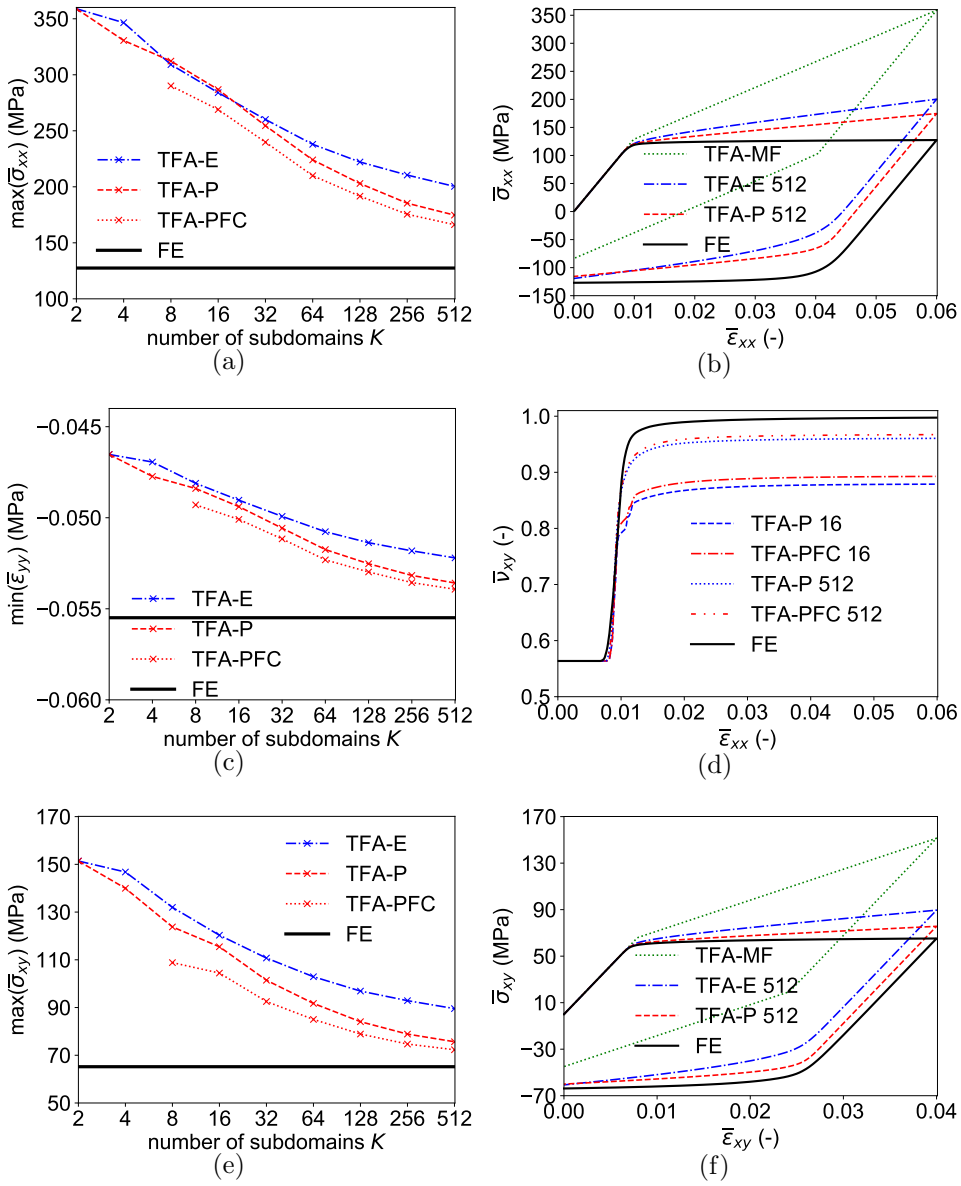

Figure 12: Normal stress response under uni-axial tension (Eq. (103)) and shear stress response under pure shear deformation (Eq. (104)) of the larger composite RVE with $v_{\mathrm{II}} = 50$ % (Fig. 11) consisting of circular stiff elastic inclusions embedded in a perfectly plastic matrix in comparison to the full-field FE result. Displayed are (a,c) the convergence of the peak stress depending on the number of subdomains and (b,d) stress-strain curves computed by the different TFA approaches.

the convergence achieved by the TFA-P is clearly better than that achieved by the TFA-E throughout the whole range of subdomains. For a number of subdomains $K = 512$, the TFA-P provides a clearly higher accuracy for the stress-strain response predictions, with an error that is less than half compared to the one achieved using the TFA-E (Figs. 12(e)

and 12(f)). The TFA-PFC results in even less stiff responses and achieves an acceptable modeling accuracy. Compared to the results achieved for the small RVE using an equal offline stage mesh size (see errors for the case $v_{\mathrm{II}} = 50\%$ with the coarse mesh in Table 1), the computation errors are lower. Therefore it is concluded, that the TFA-PFC method is not less accurate for larger RVEs.

4.3.5. Non-proportional loading conditions

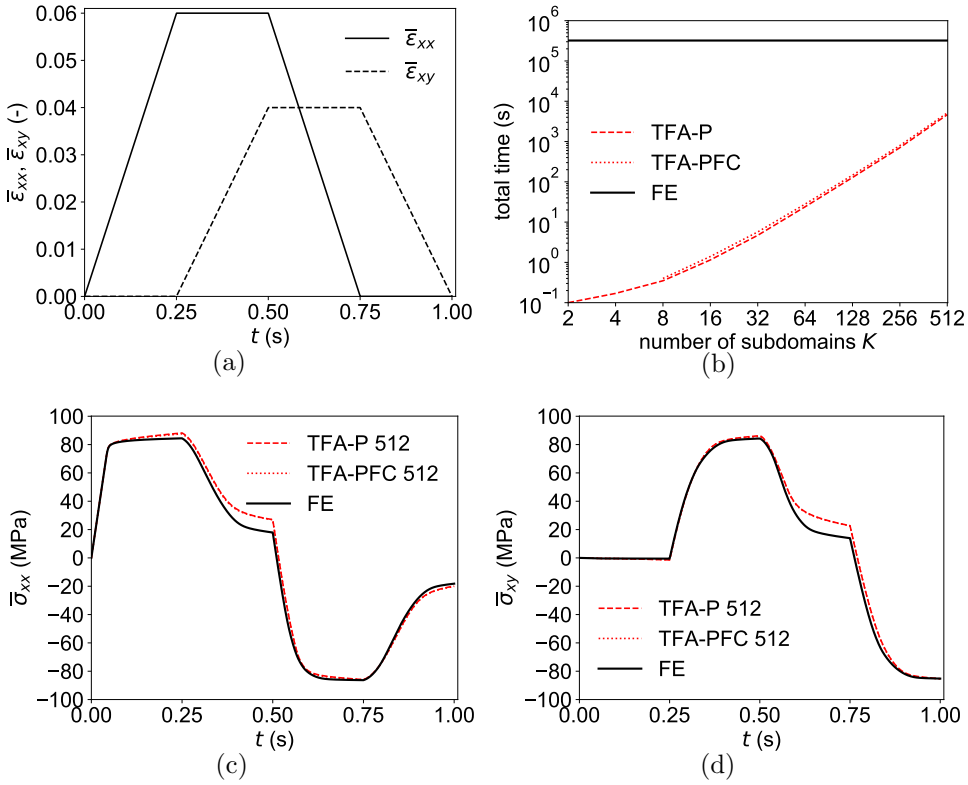

Figure 13: Non-proportional loading: Evolution of the (a) prescribed overall strain components, (b) the CPU time comparison for different subdomains numbers K and (c, d) the computed homogenized stress components predicted by the TFA-P and TFA-PFC approaches compared to the FE full-field for the composite material with $v_{\mathrm{II}} = 30$ % (Fig. 4(e-h)) consisting of circular stiff elastic inclusions embedded in an elasto-plastic matrix.

K	2	4	8	16	32	64	128	256	512
speed-up	3.2e6	1.9e6	9.2e5	2.8e5	6.8e4	1.3e4	2.5e3	460	70

Table 4: CPU time speed-ups for the non-proportional loading program in Eq. (105) using the different numbers of subdomains K for the TFA-P methods.

In order to further explore the abilities of the TFA method, an isochoric non-proportional loading program (105) displayed in Fig. 13(a) is applied to the $v_{\mathrm{II}} = 30$ % RVE consisting

of circular stiff elastic inclusions embedded in an elasto-plastic matrix (Fig. 4(e-h)). The elastic properties of the phases have a contrast $r_{\mathrm{II}} = 2$ for this application. The inelastic behavior of the matrix with the initial yield strength $\sigma_{\mathrm{I}}^{\mathrm{Y0}} = 100$ MPa follows the power-law hardening behavior

$$R = H_{\mathrm{I}}\, p^{m_{\mathrm{I}}} \tag{107}$$

with the matrix hardening modulus $H_{\mathrm{I}} = 50$ MPa and exponent $m_{\mathrm{I}} = 0.05$.

Compared are the evolutions of the different stress components predicted by the TFA-P and TFA-PFC compared to the reference full-field computations (Figs. 13(c) and 13(d)). A high accuracy of the modeled normal stress response during the applied axial deformation by the TFA-P and TFA-PFC in the stage from t=0 to $t = T/4$ is achieved. Following, inaccuracies are found considering the too low axial stress decrease during the shear loading stage from $t = T/4$ to $t = T/2$. Therefore, the predicted axial stresses have too high initial values at the start of the subsequent axial strain unloading stage from $t = T/2$ to $t = 3T/4$ but return back to the reference prediction at the end of this stage. During the final shear unloading stage from $t = 3T/4$ to $t = T$, perfect accuracies of TFA-P and TFA-PFC are maintained and therefore, correct final axial stresses are predicted. Similar observations are made for the shear stress evolution. Sole inaccuracies are found during the axial strain unloading stage from $t = T/2$ to $t = 3T/4$, where the shear stress decrease is too low. During the remaining deformation evolution, the shear stresses are correctly predicted and therefore, correct final shear stresses are predicted by both the TFA-P and TFA-PFC.

CPU time consumptions for performing the numerical analysis in Eq. (105) using the TFA algorithm with the different numbers of subdomains and the FE analysis with the same mesh as used for the offline stage simulations (27656 quadratic triangular elements), are displayed in Fig. 13(b). The computational speed-ups using the different numbers of subdomains for this 2D analysis are summarized in Table 4, providing an estimation of the possible computational savings allowed by the TFA for 2D analyses. In addition to the time savings, large CPU load reductions are provided by the use of the TFA with respect to performing full-field simulations.

4.4. Isotropic microstructures with elasto-plastic inclusions

4.4.1. Stiff elasto-plastic inclusions

Considered is an isotropic microstructure, which consists of a matrix material with circular inclusions covering a volume fraction od $\upsilon_{\mathrm{II}} = 30$ %. The elastic properties of the two phases are given in terms of the following bulk and shear moduli

- matrix: bulk modulus $\kappa_{\mathrm{I}} = 10$ GPa and shear modulus $\mu_{\mathrm{I}} = 3$ GPa;
- inclusion phase: bulk modulus $\kappa_{\mathrm{II}} = 20$ GPa and shear modulus $\mu_{\mathrm{II}} = 6$ GPa.

Both phases can deform elasto-plastically, with the yield strengths of both phases $\sigma_{\mathrm{I}}^{\mathrm{Y0}} = \sigma_{\mathrm{II}}^{\mathrm{Y0}} = 100$ MPa and a hardening behavior following the power-law relation

$$R = H_{\Omega}\, p^{m_{\Omega}}\,, \quad \Omega = \mathrm{I,II} \tag{108}$$

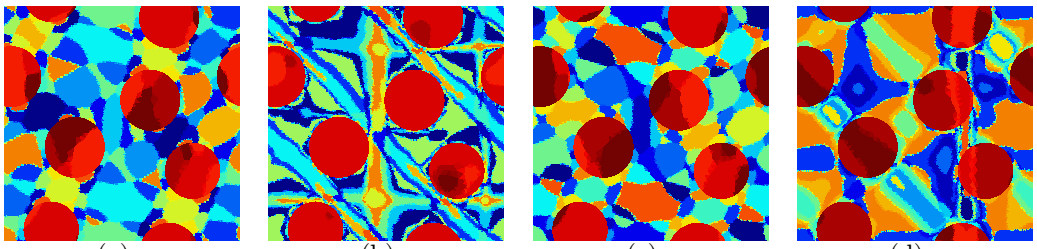

Figure 14: Microstructure and spatial decompositions of the elasto-plastic composite material with $v_{\mathrm{II}} = 30$ % of circular (a,b) stiff and (c,d) more compliant elasto-plastic inclusions based on elastic and inelastic strains into 20 subdomains, 16 of them constituting the matrix and 4 the inclusion phase.

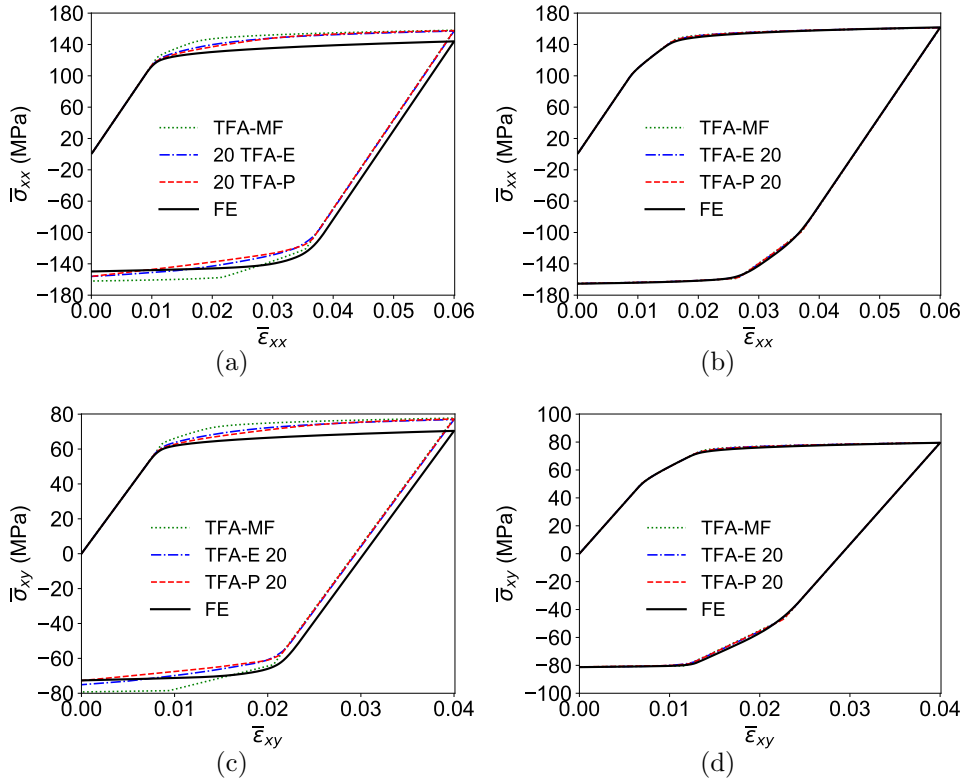

Figure 15: Normal stress response under uni-axial tension (Eq. (103)) and shear stress response under pure shear deformation (Eq. (104)) of a composite material consisting of circular stiff elasto-plastic inclusions in an elasto-plastic matrix (Fig. 14) and the different hardening exponents of the phases (a,c) $m_{\mathrm{I}} = 0.4$ and $m_{\mathrm{II}} = 0.05$ and (b,d) $m_{\mathrm{I}} = 0.05$ and $m_{\mathrm{II}} = 0.4$ resulting from the use of the different TFA approaches in comparison to the full-field FE results.

with the hardening moduli $H_{\mathrm{I}} = 50$ MPa and $H_{\mathrm{II}} = 100$ MPa and the two tested combinations of the exponents $m_{\mathrm{I}} = 0.05$, $m_{\mathrm{II}} = 0.4$ and $m_{\mathrm{I}} = 0.4$, $m_{\mathrm{II}} = 0.05$.

During the offline stage, the same mesh as in Section 4.3 was used. The material prop-

erties used during the inelastic offline stage simulations for a material consisting of stiff elasto-plastic inclusions in an elasto-plastic matrix are given in Section 4.1. As previously, diagonal and axially-oriented inelastic bands, crossing the material on inter-inclusion paths, are formed during the bi-axial and the pure shear deformation modes, respectively. The inelastic deformations in the inclusions are not connected to the shear bands. The RVE was divided into $K = 20$ subdomains, where the matrix phase is composed of 16 and the inclusion phase of four subdomains. The spatial RVE decompositions based on elastic and plastic strain distributions are depicted in Figs. 14(a) and 14(b). The plasticity-based spatial subdivision approach allows covering deformation patterns corresponding to the same general shear band orientations and their intersecting regions in the matrix phase as in the considerations of elastic inclusions.

The resulting strain-stress responses are displayed in Fig. 15. Very high accuracies are accomplished with the TFA-MF approach, using only one subdomain per material phase (green curves). The full-field solution is nearly perfectly recovered by the TFA-E and TFA-P in the cases of a low hardening exponent in the more compliant matrix phase and a high hardening exponent in the stiffer inclusion phase (Figs. 15(b) and 15(d)). Less accurate results represented by a slightly over-stiff behavior compared to the full-field solution are predicted using the TFA-E and TFA-P in the case of a high hardening exponent in the matrix phase and a low hardening exponent in the inclusion phase (Figs. 15(a) and 15(c)). In this case, the TFA-P with more subdomains allows predictions with slightly increased proximity to the full-field results compared to the TFA-MF in the low-strain regime. However, the stress responses appear to converge towards the TFA-MF solution under an increasing strain.

4.4.2. Compliant elasto-plastic inclusions

Now, the role of the two materials are reversed compared to the case considered in Section 4.4.1, meaning that the stiff material constitutes the matrix phase and the more compliant material the inclusion phase, represented in terms of the elastic properties

- matrix: bulk modulus $\kappa_{\mathrm{I}} = 20$ GPa and shear modulus $\mu_{\mathrm{I}} = 6$ GPa;
- inclusion phase: bulk modulus $\kappa_{\mathrm{II}} = 10$ GPa and shear modulus $\mu_{\mathrm{II}} = 3$ GPa.

Accordingly, the inelastic properties are reversed, implying a power-law hardening behavior (Eq. (108)) of the corresponding phases governed by $\sigma_{\mathrm{I}}^{\mathrm{Y0}} = \sigma_{\mathrm{II}}^{\mathrm{Y0}} = 100$ MPa, the hardening moduli $H_{\mathrm{I}} = 100$ MPa and $H_{\mathrm{II}} = 50$ MPa and the two combinations of the exponents $m_{\mathrm{I}} = 0.05$, $m_{\mathrm{II}} = 0.4$ and $m_{\mathrm{I}} = 0.4$, $m_{\mathrm{II}} = 0.05$.

During the inelastic offline stage simulations (performed with the same mesh as in Section 4.3 and the inelastic material properties for a material with compliant elasto-plastic inclusions in an elasto-plastic matrix given in Section 4.1), the inelastic deformation localizes in band-like patterns, oriented diagonally caused by bi-axial isochoric and axially caused by pure shear overall deformation. Different from the case of stiff elasto-plastic inclusions (Figs. 14(a) and 14(b)), the inclusions are now integrated in the plastic shear bands. The resulting subdomain decompositions into a total of 20 subdomains based on elasticity and plasticity are presented in Figs. 14(c) and 14(d), where the matrix phase is constituted by

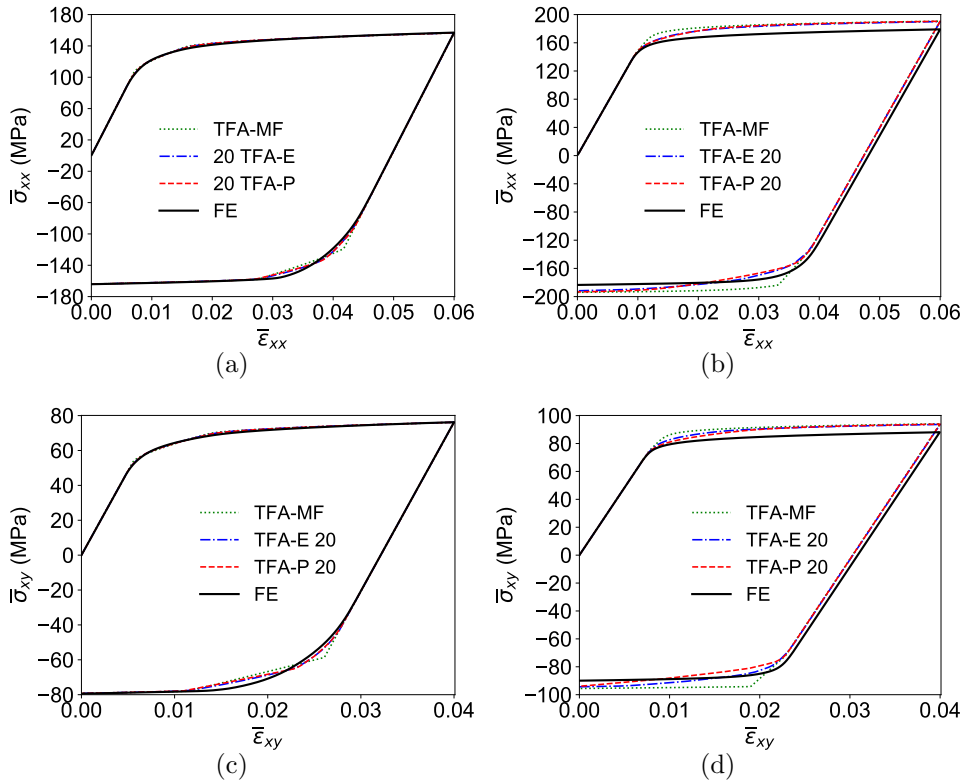

Figure 16: Normal stress response under uni-axial tension (Eq. (103)) and shear stress response under pure shear deformation (Eq. (104)) of a composite material consisting of circular more compliant elasto-plastic inclusions in an elasto-plastic matrix (Fig. 14) and the different hardening exponents of the phases (a,c) $m_{\mathrm{I}} = 0.4$ and $m_{\mathrm{II}} = 0.05$ and (b,d) $m_{\mathrm{I}} = 0.05$ and $m_{\mathrm{II}} = 0.4$ resulting from the use of the different TFA approaches in comparison to the full-field FE results.

16 subdomains and the inclusion phase by four subdomains. With inclusions considered being more compliant than the matrix phase, the subdomain patterns using plastic strain distributions do not avoid but connect through the inclusions.

The axial stress response under uni-axial tension and the shear stress response under pure shear conditions are presented in Fig. 16. Again, the TFA-MF yields accurate predictions and the full-field results are nearly exactly reproduced by the TFA-E and TFA-P in the cases of a low hardening exponent in the more compliant phase, here the inclusion phase (Figs. 16(a) and 16(c)). The modeled behavior using the TFA-E and TFA-P is slightly overstiff in comparison with the full-field result only in case of a high hardening exponent in the more compliant phase (Figs. 16(b) and 16(d)).

4.5. Anisotropic microstructures and material behavior

The two anisotropic microstructures consist of a matrix with elliptic, purely-elastic inclusions, covering a volume fraction $v_{\mathrm{II}} = 20$ %. The degree of anisotropy represented by the ratio of the radii r_x and r_y of the elliptic inclusions differs for the two microstructures: they

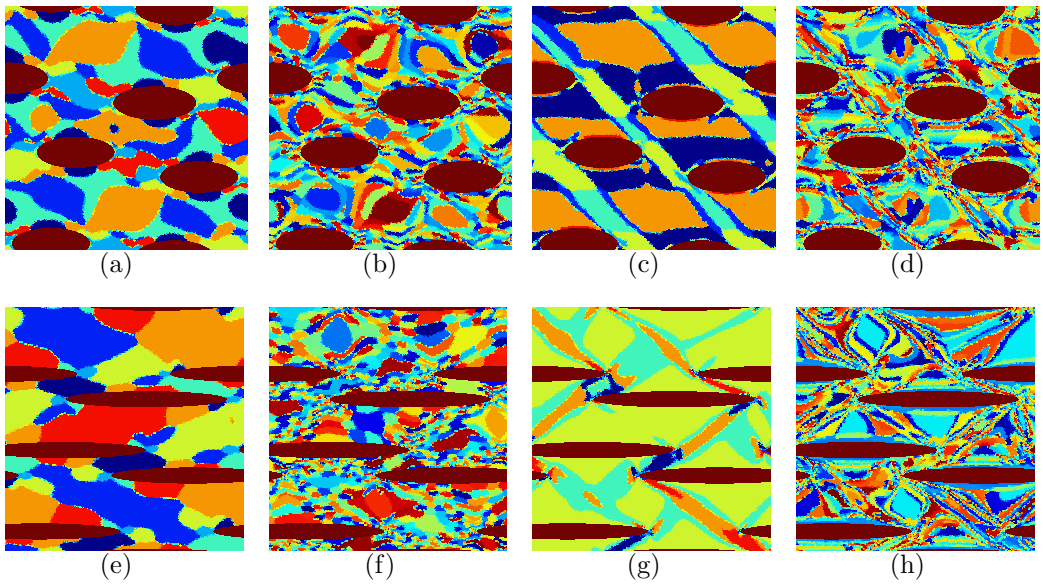

Figure 17: Microstructure and spatial decompositions of the composite material with an anisotropic structure with $v_{\text{II}} = 20\%$ of elliptic stiff and anisotropic elastic inclusions with (a-d) aspect ratio $r_x/r_y = 2.5$ and (e-h) aspect ratio $r_x/r_y = 10$ in an elasto-plastic matrix based on elastic deformation into (a, e) 8 subdomains and (c, g) 128 subdomains and based on inelastic deformation into (b, f) 8 subdomains and (d, h) 128 subdomains.

$r_x/r_y = 1$	TFA-E 512	TFA-P 512	TFA-PFC 512
e_{xx} (%)	9	5	4
e_{xy} (%)	8	2	2
$r_x/r_y = 2.5$	TFA-E 512	TFA-P 512	TFA-PFC 512
e_{xx} (%)	11	6	5
e_{xy} (%)	4	2	1
$r_x/r_y = 10$	TFA-E 512	TFA-P 512	TFA-PFC 512
e_{xx} (%)	17	13	10
e_{yy} (%)	10	4	3
e_{xy} (%)	1	1	1

Table 5: Peak stress errors (computed as in Eq. (106)) using the different TFA approaches for the composite material with an anisotropic microstructure and $v_{\text{II}} = 20\%$ (Fig. 17) consisting of elliptic stiff elastic inclusions embedded in a perfectly plastic matrix.

are successively taken as $r_x/r_y = 2.5$ and $r_x/r_y = 10$, with the elongations along the x-axis orientation. The material system consists of an elasto-J_2-plastic matrix material with the elastic and inelastic material properties as in Section 4.3 and stiff linear-elastic inclusions with the transverse-isotropic (or "polar-anisotropic") properties

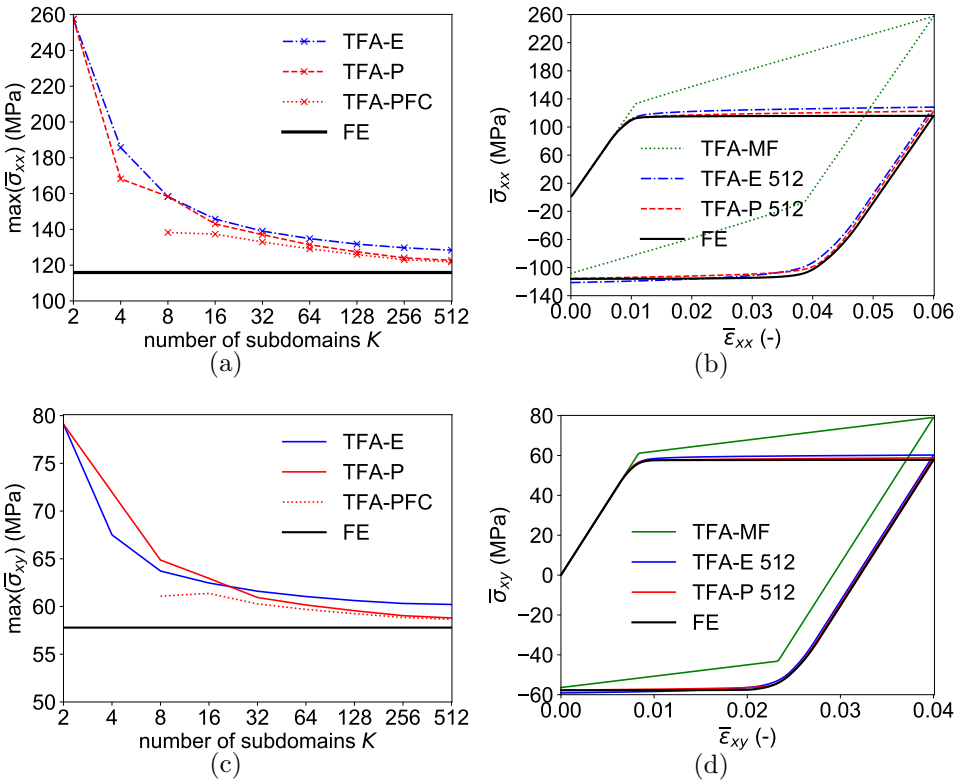

Figure 18: Normal stress response under uni-axial tension in x-direction (longitudinal loading, Eq. (103)) and shear stress response under pure shear deformation (Eq. (104)) of a composite material with an anisotropic microstructure of $v_{\mathrm{II}} = 20\%$ (Fig. 17(a-d)) elliptic stiff and anisotropic elastic inclusions aspect ratio $r_x/r_y = 2.5$ embedded in a perfectly plastic matrix in comparison to the full-field FE result. Displayed are (a, c) the convergence of the peak stress depending on the number of subdomains and (b, d) stress-strain curves computed by the different TFA approaches.

- $E_x = 40$ GPa, $E_y = E_z = 10$ GPa
- $\nu_{xy} = \nu_{xz} = 0.24$, $\nu_{yz} = 0.3333$,
- $\mu_{xy} = \mu_{xz} = 8$ GPa, $\mu_{yz} = \frac{E_y}{2\,(1+\nu_{yz})} = 3.75$ GPa

where the inclusion phase subscript "II" is omitted for the simplicity of notation. Additionally to the uni-axial tension text in longitudinal fiber direction and the pure shear test, a transverse uni-axial tension test with up to $\overline{\boldsymbol{\varepsilon}}_{yy} = 3\%$ (exchange of xx and yy in Eq. (103)) was applied on the RVE with the high inclusion aspect ratio. The computation errors of the tension in y-direction are denoted as e_{yy}.

4.5.1. Spatial division into subdomains

The offline stage simulations were performed using meshes consisting of 30018 and 34326 triangular quadratic elements for the microstructure with the lower degree of anisotropy

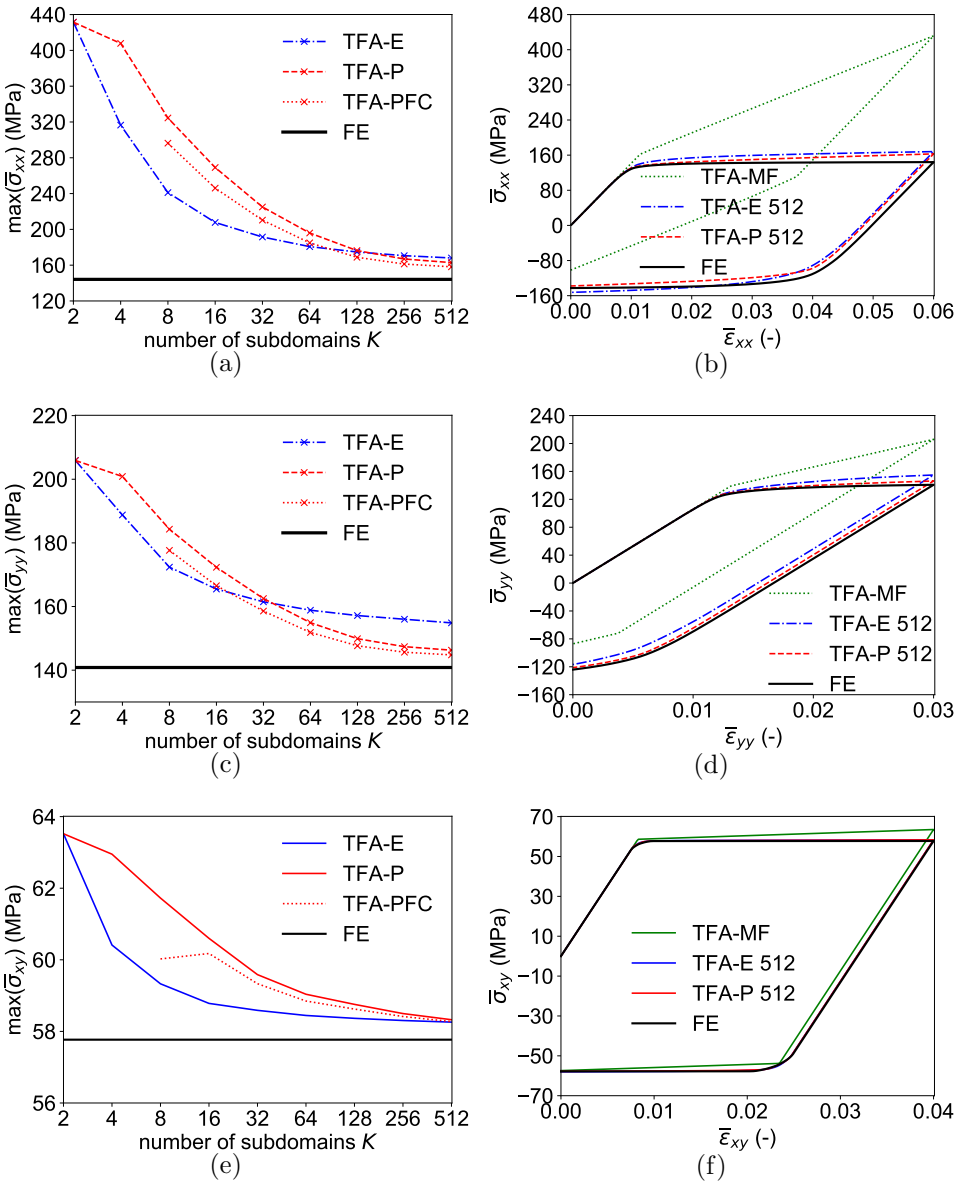

Figure 19: Normal stress responses under uni-axial tension in x-direction (longitudinal loading, Eq. (103)) and in y-direction (transverse loading) and shear stress response under pure shear deformation (Eq. (104)) of a composite material with a higly anisotropic microstructure of $v_{\mathrm{II}} = 20\%$ (Fig. 17(e-h)) elliptic stiff and anisotropic elastic inclusions aspect ratio $r_x/r_y = 10$ embedded in a perfectly plastic matrix in comparison to the full-field FE result. Displayed are (a, c, e) the convergence of the peak stress depending on the number of subdomains and (b, d, f) stress-strain curves computed by the different TFA approaches.

and the one used for the strong isotropic microstructure, respectively. The inelastic material properties of the elasto-plastic matrix during the offline stage simulations are the ones given in Section 4.1 for the material system of elastic inclusions in an elasto-plastic matrix. The inclusions anisotropic elastic behavior is described by the previously introduced elastic

properties. In the case of the microstructure with the lower anisotropy $r_x/r_y = 2.5$, the inelastic deformations under the bi-axial deformation and pure shearing are carried by a low number of wide shear bands, traversing the material in diagonal and axial directions, as recognized in the spatial decomposition (Fig. 17(c,d)). In the case of a strong anisotropy expressed by $r_x/r_y = 10$, the inelastic patterns differ from the previously considered cases. Under the bi-axial isochoric deformation, plastic localizations form around and between the sharp peaks of the inclusions. Under pure shearing, plastic strain localizes in longitudinal direction and particularly along the long inclusion edges (see Fig. 17(g,h)), while the regions between the inclusion peaks are almost spared by the occurrence of plasticity. The RVE domains were divided in the offline stage into $K = 2$, 16, 32, 64, 128, 256, 512 subdomains, with one subdomain representing the elastic inclusion phase. The microstructures and the spatial decompositions resulting from elastic and inelastic deformation into 8 and 128 subdomains are presented in Fig. 17(a-d) for the lower anisotropy $r_x/r_y = 2.5$ and in Fig. 17(e-h) for the higher anisotropy $r_x/r_y = 10$.

4.5.2. Perfectly plastic matrix material with linear-elastic, transverse-isotropic inclusions

The matrix material behaves perfectly plastic with the yield strength $\sigma_{\mathrm{I}}^{\mathrm{Y0}} = 100$ MPa, while the inclusions deform linearly-elastic with the transverse-isotropic elastic properties given above. In case of the lower degree of anisotropy, the TFA-P provides a better convergence towards the reference result than the TFA-E throughout the whole range of the numbers of subdomains for the uni-axial tension test and for $K \geq 32$ for the pure shear test. The TFA-PFC yields additional improvements of accuracy in the region of low numbers of subdomains. It is recognized that peak stress errors are low using TFA-E but can still be significantly reduced using the TFA-P and TFA-PFC (Table 5 and Figs. 18(a) and 18(c)). Therefore, the stress-strain responses computed by the TFA-P and TFA-PFC with 512 subdomains show negligible deviations from the reference full-field stress-strain responses under uni-axial tension and pure shearing (Figs. 18(b) and 18(d)).

In case of the strong anisotropic microstructure, the TFA-E provides more accurate results than the TFA-P and TFA-PFC for a wide range of subdomains for both the uni-axial tension and the pure shear tests (Figs. 19(a), 19(c) and 19(e)). In the uni-axial tests, the TFA-P and TFA-PFC show a higher convergence rate towards the reference results and allow more accurate predictions for respectively $K \geq 128$ and $K \geq 32$. With 512 subdomains, the peak stress error is slightly in the longitudinal tension and significantly in the transverse tension test reduced using the TFA-P and the TFA-PFC (Table 5), visible in the computed stress-strain responses (Figs. 19(b) and 19(d)). In the pure shear test, the computation errors are negligible using all three TFA methods with a sufficiently high number of subdomains (Fig. 19(e) Fig. 19(f)).

4.6. Evaluation of the achieved results

If a two-phase microstructure is considered where both phases deform inelastically, the TFA with only one subdomain per phase, referred to as TFA-MF, provides accurate stress-strain predictions (see Sections 4.4.1 and 4.4.2). Issues occur if the inclusion phase deforms purely elastic and the matrix phase deforms inelastically with low hardening characteristics.

The modeled over-stiff behavior is a result of over-estimated instantaneous strain concentrations in the stiff phases and under-estimated strain concentrations in the inelastically deforming phases during inelastic deformation of the material. Over-estimated strain and therefore stress accumulations in stiff phases cause, following Eq. (96), over-estimated composite stress responses.

The issue of an over-estimated tangent behavior can as well be analysed by a consideration of the composite tangent stiffness, computed as in Eq. (100). Following Eq. (100), the error in the overall tangent stiffness is explained by inaccurate instantaneous strain concentration tensors $\mathbb{A}_r^{\text{in}}$. As visible in Eq. (99) with Eq. (93), the $\mathbb{A}_r^{\text{in}}$ are directly dependent of the term $\mathbb{D}_{rs} : \partial \Delta \boldsymbol{\varepsilon}_s^* / \partial \boldsymbol{\varepsilon}_s$. Inaccuracies in the spatial capture of the inelastic interaction field due to an averaging over subdomains (Section 3.3), and hence insufficient contributions of the term $\mathbb{D}_{rs} : \partial \Delta \boldsymbol{\varepsilon}_s^* / \partial \boldsymbol{\varepsilon}_s$, are the cause of inaccurate instantaneous strain concentrations during the TFA computation.

If the matrix phase has a perfectly plastic mechanical behavior, it carries all deformation in the material and the inclusions undergo no strain. The concentration of the entire overall strain in the matrix phase and zero strain in the inclusions can, using the TFA approach, solely be successfully modeled if the interaction field is fully captured by the spatial decomposition, meaning that the case of elastic inclusions in a perfectly plastic matrix is a highly-complex material system. In composite materials with heterogeneous micro-structures, a capture of the full highly-heterogeneous plastic field is impossible using numbers of subdomains that are reasonably low, leading naturally to incorrect instantaneous strain distributions and an over-estimated tangent behavior by the TFA method.

The mechanical predictions using the TFA for composite materials consisting of purely elastic inclusions in a perfectly plastic matrix could be significantly improved with an optimized subdomain decomposition which bases on inelastic fields compared to a subdomain decomposition based on elastic fields (see Sections 4.3 and 4.5). The enhanced representation of the real interaction field by means of an inelasticity-based subdomain decomposition results in more accurate strain distributions over the material phases during the online stage and therefore allows an improved TFA modeling accuracy. The quality of the TFA modeling and the improvement of the enhanced spatial decomposition with respect to the spatial decomposition based on elasticity were quantified with regard of the following influences: the volume fractions of the stiff inclusion phases, the degree of microstructure anisotropy and the contrast between the phase stiffnesses. The TFA provides accurate results with errors $< 10\%$ for the cases of low or moderate inclusion volume fractions $\upsilon_{\text{II}} = 20\%$ and 30%. Further it is shown that the subdomain decomposition based on inelastic fields under proportional deformation modes holds for loading-unloading cycles as well as for a non-proportional loading path consisting of four consecutive deformation stages (see Section 4.3.5). The proposed fluctuation correction (denoted as TFA-PFC) has a positive impact on the achieved TFA modeling results of elastic inclusions in a perfectly plastic matrix due to the artificially increased interaction effects in Eq. (93).

High prediction errors with up to 512 subdomains are encountered for a high inclusion phase volume fraction $\upsilon_{\text{II}} = 50\%$. It appears that the TFA errors are increasing as a function of the inclusion volume fraction. This can be explained as follows: First, the heterogeneity

of the plastic field increases in case of higher volume fractions of inclusions, making the efficient representation of the plastic field by an averaging procedure more complex. Second, the inability of the TFA method to avoid occurring strains in stiff inclusions becomes more severe the higher the volume fraction of inclusions. Higher numbers of subdomains may lead to more accurate results, but at the same time, extremely fine meshes are required for the k-means clustering to identify meaningful subdomains when such high numbers of subdomains are used, resulting in more time-expansive offline and online stages.

5. Conclusions

The TFA based two-scale ROM approach for heterogeneous composite materials is investigated in this paper for a range of 2D micro-structures. Since the TFA does not rely on the stiffness of a homogeneous (and isotropic) reference material, it is assumed to provide reliable mechanical predictions for general composite materials. However, the TFA approach using piece-wise uniform fields is known to yield over-stiff approximations for the inelastic mechanical behavior of composites, especially in cases of high localized plasticity when using reasonably low numbers of subdomains. The reason for computed over-stiff composite predictions by the TFA-ROM is an insufficiently accurate distribution of the overall strain over the subdomains, resulting in over-predicted strain and stress accumulations in stiff or elastic phases during inelastic deformation of the composite. Not ideally determined eigenstrain-strain interaction tensors between subdomains, and therefore under-estimated overall eigenfield influences were identified as a cause for incorrect strain distributions over the material phases (more detailed in Sections 3.3 and 4.6).

Formerly proposed two-scale approaches achieving a model order reduction by using piece-wise uniform fields often use elastic strain distributions as the foundation for the spatial decomposition, proven to result in improved mechanical predictions in comparison to the use of spatially regular subdomain decompositions (Liu et al., 2016; Wulfinghoff et al., 2018). In this work it was recognized, that the consideration of inelastic micro-mechanical deformation patterns can provide an improved modeling using piece-wise uniform field ROM approaches. This new approach for the spatial decomposition provides a more physics-based modeling respecting the real micromechanics due to an increased emphasis on the main features of the inelastic and therefore of the interaction field. Inelastic deformation patterns evolving due to plastic localization, often particularly in the form of plastic shear bands, are not detectable and therefore not respected by purely elastic pre-analyses. It is successfully shown that the predictions for the strain-stress responses for the more complex case of elastic inclusions in an elasto-plastic matrix can be improved by using the enhanced subdomain decomposition based on inelastic deformation fields.

Very accurate results using low numbers of subdomains are achieved for two-phase composite materials with two inelastically deforming material phases. Clear improvements of the TFA predictions and accurate modeling results using the enhanced spatial division are achieved for the very demanding cases of elastic inclusions in a perfectly plastic matrix phase for low to moderate volume fractions of inclusions v_{II}. The high TFA prediction quality is valid for heterogeneous composites materials with isotropic and anisotropic microstructures

and material properties, as well as for different degrees of the phases elastic stiffness contrasts.

However, the error of the tangent behavior of composite materials increases with an increasing inclusion volume fraction as discussed in Section 4.6. The TFA predictions for the tangent behavior of composite materials with $v_{\mathrm{II}} = 50\%$ in this work are still over-stiff for 512 subdomains defined using the inelasticity-based spatial decomposition, although the error continues to decrease with an increasing number of subdomains, provided the mesh used during the offline stage is fine enough.

The use of statistical field inhomogeneities is a first micromechanics-based correction approach for the modeling of composite materials based on piece-wise uniform fields. Although it is shown to provide an additional acceleration of the convergence of the achieved strain-stress responses by the TFA towards the reference full-field results, further work is required in order to optimize the use of in-subdomain field fluctuations for an efficient improvement of the inelastic response of composite materials.

The offline stage in this work consists of two RVE deformation modes. More deformation modes can be included in the offline stage, allowing the enhanced inelasticity-based TFA modeling of materials under arbitrary loading conditions. A higher number of offline deformation modes might lead to the requirement of higher numbers of subdomains in order to properly cover the various deformation patterns inside the RVE. Consequently, approaches for adapted subdomain decompositions achieved by either using pre-computed load-specific sets of subdomains or performing re-clustering procedures during the online stage may be considered in the future.

Acknowledgement

The research has been funded by the Walloon Region under the agreement n^o.7911-VISCOS in the context of the 21st SKYWIN call.

Data availability

The raw/processed data required to reproduce these findings cannot be shared at this time as the data also forms part of an ongoing study.

Appendix A. Derivatives of the incremental stress-strain response using the J_2-plasticity model

In the following, the derivative of the incremental stress-strain response computed by the J_2-plasticity model are given. The stress tensor is computed as

$$\boldsymbol{\sigma} = \boldsymbol{\sigma}^{\mathrm{tr}} - 2G^{\mathrm{el}}\Delta\boldsymbol{\varepsilon}^{\mathrm{p}} = \boldsymbol{\sigma}^{\mathrm{tr}} - 2G^{\mathrm{el}}\Delta p\boldsymbol{N}. \tag{A.1}$$

Derivatives with respect to the strain (it is noted that $\partial\square/\partial\Delta\boldsymbol{\varepsilon} = \partial\square/\partial\boldsymbol{\varepsilon}$) follow from the derivatives

$$\frac{\partial\boldsymbol{\sigma}^{\mathrm{tr}}}{\partial\boldsymbol{\varepsilon}} = \mathbb{C}^{\mathrm{el}}, \tag{A.2}$$

$$\frac{\partial \Delta p}{\partial \boldsymbol{\varepsilon}} = \frac{2G^{\mathrm{el}}}{h}\boldsymbol{N}, \tag{A.3}$$

and

$$\frac{\partial \boldsymbol{N}}{\partial \boldsymbol{\varepsilon}} = \frac{\partial \boldsymbol{N}}{\partial \boldsymbol{\sigma}^{\mathrm{tr}}} : \frac{\partial \boldsymbol{\sigma}^{\mathrm{tr}}}{\partial \boldsymbol{\varepsilon}} = \frac{1}{\sigma^{\mathrm{tr,eq}}}\left(\frac{3}{2}\mathbb{I}^{\mathrm{dev}} - \boldsymbol{N}\otimes\boldsymbol{N}\right) : \mathbb{C}^{\mathrm{el}} = \frac{2G^{\mathrm{el}}}{\sigma^{\mathrm{tr,eq}}}\left(\frac{3}{2}\mathbb{I}^{\mathrm{dev}} - \boldsymbol{N}\otimes\boldsymbol{N}\right), \tag{A.4}$$

where

$$h = 3G^{\mathrm{el}} + \partial R/\partial p. \tag{A.5}$$

These expressions result into the expression of the plastic strain derivative

$$\frac{\partial \Delta \boldsymbol{\varepsilon}^{\mathrm{p}}}{\partial \boldsymbol{\varepsilon}} = \frac{2G^{\mathrm{el}}}{h}\boldsymbol{N}\otimes\boldsymbol{N} + 2G^{\mathrm{el}}\frac{\Delta p}{\sigma^{\mathrm{tr,eq}}}\left(\frac{3}{2}\mathbb{I}^{\mathrm{dev}} - \boldsymbol{N}\otimes\boldsymbol{N}\right), \tag{A.6}$$

and into the expression of the algorithmic tangent

$$\mathbb{C}^{\mathrm{tan}} = \mathbb{C}^{\mathrm{el}} - 2G^{\mathrm{el}}\frac{\partial \Delta \boldsymbol{\varepsilon}^{\mathrm{p}}}{\partial \boldsymbol{\varepsilon}} = \mathbb{C}^{\mathrm{el}} - \frac{(2G^{\mathrm{el}})^2}{h}\boldsymbol{N}\otimes\boldsymbol{N} - (2G^{\mathrm{el}})^2\frac{\Delta p}{\sigma^{\mathrm{tr,eq}}}\left(\frac{3}{2}\mathbb{I}^{\mathrm{dev}} - \boldsymbol{N}\otimes\boldsymbol{N}\right). \tag{A.7}$$

Appendix B. Convergence study of the overall deformation factor $\boldsymbol{E}^{\mathrm{in}}$ for the inelastic deformation modes

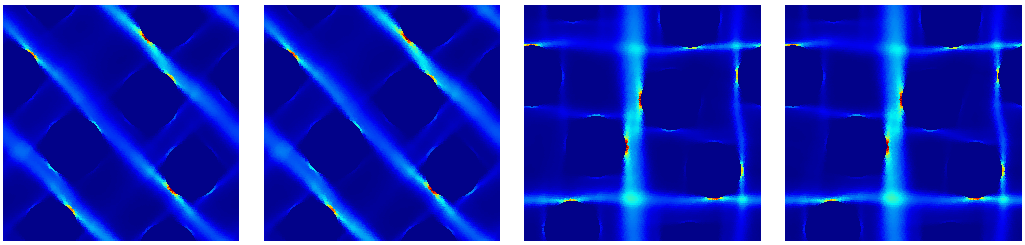

(a) (b) (c) (d)

Figure B.20: Equivalent plastic field patterns inside the RVE with $v_{\mathrm{II}} = 30\,\%$ of circular stiff elastic inclusions in an elasto-plastic matrix under the two deformation modes (a, b) $l = 1$ and (c, d) $l = 2$ (Eq. (65)) with the deformation factors (a, c) $E^{\mathrm{in}} = 2\%$ and (b, d) $E^{\mathrm{in}} = 8\%$.

In this section, the justification of the overall deformation factor for the inelastic offline deformation modes $E^{\mathrm{in}} = 2\%$ is presented by means of a convergence study using the RVE with $v_{\mathrm{II}} = 30\ \%$ of circular stiff elastic inclusions in an elasto-plastic matrix. The k-means clustering method is based on the differences of local quantities, and is therefore sensitive to spatial distributions rather than the particular magnitudes of the local quantity. In order to achieve a clustering into subdomains that does not change if the overall deformation increases, it is important that the final spatial plastic field configurations are achieved under the offline deformation modes. Thus, the overall deformation factor for the inelastic offline

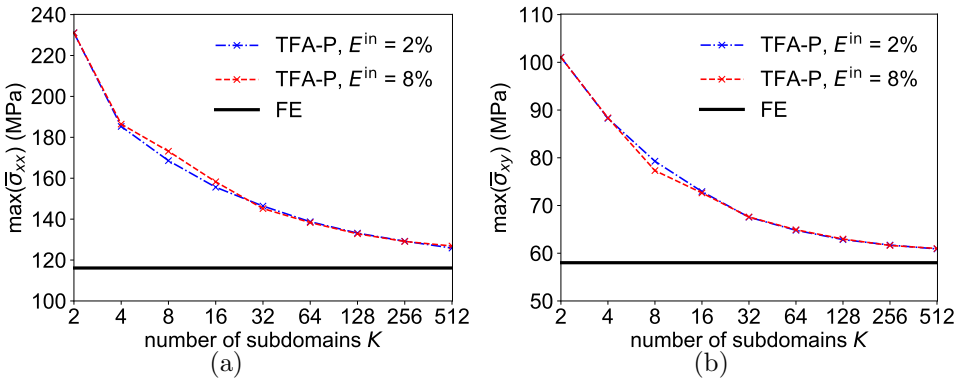

Figure B.21: The convergence of the (a) peak normal stress under uni-axial tension (Eq. (103)) and of the (b) peak shear stress under pure shear deformation (Eq. (104)) depending on the number of subdomains for the RVE with $v_{\mathrm{II}} = 30$ % of circular stiff elastic inclusions in an elasto-plastic matrix. Compared are the use of the TFA-P using subdomains computed with the offline deformation factors $E^{\mathrm{in}} = 2\%$ and $E^{\mathrm{in}} = 8\%$.

simulations was selected with the goal to be just high enough to achieve the final spatial plastic patterns in the composite RVEs with the material properties given in Section 4.1.

According to Fig. B.20, the achieved plastic patterns under both deformation modes in Eq. (65) with the overall deformation factors $E^{\mathrm{in}} = 2\%$ and $E^{\mathrm{in}} = 8\%$ are identical, implying that final plastic field patterns are established under the selected deformation factor $E^{\mathrm{in}} = 2\%$. We note that the clustering is achieved by considering the plastic strain tensor components and not the equivalent plastic strain scalar, but for readability Fig. B.20 displays a scalar value. Additionally, the achieved TFA results for the uni-axial tension and the pure-shear tests in Eqs. (103) and (104) using the subdomain decomposition based on the two offline deformation factors are compared in Fig. B.21. It is visible that the deviations between the two results are negligible. Based on this, it can be concluded that the RVE deformation of 2 % in combination with the mentioned material properties is sufficient to achieve the final plastic field patterns in the offline stage.

References

Aboudi, J., Arnold, S.M., Bednarcyk, B.A., 2013. Chapter 3 - Fundamentals of the Mechanics of Multiphase Materials. Butterworth-Heinemann, Oxford. pp. 87–145. URL: https://www.sciencedirect.com/science/article/pii/B9780123970350000033, doi:https://doi.org/10.1016/B978-0-12-397035-0.00003-3.

Caicedo, M., Mroginski, J.L., Toro, S., Raschi, M., Huespe, A., Oliver, J., 2019. High performance reduced order modeling techniques based on optimal energy quadrature: Application to geometrically non-linear multiscale inelastic material modeling. Archives of Computational Methods in Engineering 26, 771–792. doi:10.1007/s11831-018-9258-3.

Castrogiovanni, A., Marfia, S., Auricchio, F., Sacco, E., 2021. Tfa and hs based homogenization techniques for nonlinear composites. International Journal of Solids and Structures 225, 111050. URL: https://www.sciencedirect.com/science/article/pii/S0020768321001347, doi:https://doi.org/10.1016/j.ijsolstr.2021.111050.

Cavaliere, F., Reese, S., Wulfinghoff, S., 2020. Efficient twoscale simulations of engineering structures using the hashinshtrikman type finite element method. Computational Mechanics 65, 159 – 175. URL: https://www.springerprofessional.de/en/efficient-two-scale-simulations-of-engineering-structures-using-/17118994, doi:10.1007/s00466-019-01758-4.

Chaboche, J., Kanouté, P., Roos, A., 2005. On the capabilities of mean-field approaches for the description of plasticity in metal matrix composites. International Journal of Plasticity 21, 1409–1434. URL: https://www.sciencedirect.com/science/article/pii/S0749641904001433, doi:https://doi.org/10.1016/j.ijplas.2004.07.001.

Chaboche, J., Kruch, S., Maire, J., Pottier, T., 2001. Towards a micromechanics based inelastic and damage modeling of composites. International Journal of Plasticity 17, 411–439. URL: https://www.sciencedirect.com/science/article/pii/S0749641900000565, doi:https://doi.org/10.1016/S0749-6419(00)00056-5.

Charalambakis, N., 2010. Homogenization Techniques and Micromechanics. A Survey and Perspectives. Applied Mechanics Reviews 63. URL: https://doi.org/10.1115/1.4001911, doi:10.1115/1.4001911, arXiv:https://asmedigitalcollection.asme.org/appliedmechanicsreviews/article-pdf/63/3/030803/5442740

Covezzi, F., de Miranda, S., Marfia, S., Sacco, E., 2016. Complementary formulation of the tfa for the elasto-plastic analysis of composites. Composite Structures 156, 93–100. URL: https://www.sciencedirect.com/science/article/pii/S0263822316001173, doi:https://doi.org/10.1016/j.compstruct.2016.01.094. 70th Anniversary of Professor J. N. Reddy.

Doghri, I., Brassart, L., Adam, L., Gérard, J.S., 2011. A second-moment incremental formulation for the mean-field homogenization of elasto-plastic composites. International Journal of Plasticity 27, 352–371. URL: https://www.sciencedirect.com/science/article/pii/S0749641910000835, doi:10.1016/j.ijplas.2010.06.004.

Dvorak, G., Bahei-El-Din, Y., Wafa, A., 1994. Implementation of the transformation field analysis for inelastic composite materials. Computational Mechanics 14, 201–228. URL: https://link.springer.com/article/10.1007%2FBF00370073, doi:10.1007/BF00370073.

Dvorak, G.J., 1990. On uniform fields in heterogeneous media. Proceedings of the Royal Society of London. Series A: Mathematical and Physical Sciences 431, 89–110. URL: https://royalsocietypublishing.org/doi/10.1098/rspa.1990.0120, doi:10.1098/rspa.1990.0120, arXiv:https://royalsocietypublishing.org/doi/pdf/10.1098/rspa.1990.0120.

Dvorak, G.J., 1992. On transformation strains and uniform fields in multiphase elastic media. Proceedings of the Royal Society of London. Series A: Mathematical and Physical Sciences 437, 291–310. URL: https://royalsocietypublishing.org/doi/10.1098/rspa.1992.0062, doi:10.1098/rspa.1992.0062, arXiv:https://royalsocietypublishing.org/doi/pdf/10.1098/rspa.1992.0062.

Feyel, F., 1999. Multiscale fe2 elastoviscoplastic analysis of composite structures. Computational Materials Science 16, 344–354. URL: https://www.sciencedirect.com/science/article/pii/S0927025699000774, doi:10.1016/S0927-0256(99)00077-4.

Fish, J., Shek, K., Pandheeradi, M., Shephard, M., 1997. Computational plasticity for composite structures based on mathematical homogenization: Theory and practice. Computer Methods in Applied Mechanics and Engineering 148, 53 – 73. doi:10.1016/S0045-7825(97)00030-3.

Fritzen, F., Leuschner, M., 2013. Reduced basis hybrid computational homogenization based on a mixed incremental formulation. Computer Methods in Applied Mechanics and Engineering 260, 143–154. URL: https://www.sciencedirect.com/science/article/pii/S0045782513000583, doi:10.1016/j.cma.2013.03.007.

Gajek, S., Schneider, M., Böhlke, T., 2020. On the micromechanics of deep material networks. Journal of the Mechanics and Physics of Solids 142, 103984. doi:10.1016/j.jmps.2020.103984.

Geers, M., Kouznetsova, V., Brekelmans, W., 2010. Multi-scale computational homogenization: Trends and challenges. Journal of Computational and Applied Mathematics 234, 2175–2182. URL: https://www.sciencedirect.com/science/article/pii/S0377042709005536, doi:https://doi.org/10.1016/j.cam.2009.08.077. fourth International Conference on Advanced COmputational

Methods in ENgineering (ACOMEN 2008).
Geers, M.G.D., Kouznetsova, V.G., Matou, K., Yvonnet, J., 2017. Homogenization Methods and Multiscale Modeling: Nonlinear Problems. Wiley. pp. 1–34. URL: https://onlinelibrary.wiley.com/doi/abs/10.1002/9781119176817.ecm2107, doi:10.1002/9781119176817.ecm2107, arXiv:https://onlinelibrary.wiley.com/doi/pdf/10.1002/9781119176817.ecm2107.
Hernández, J., Oliver, J., Huespe, A., Caicedo, M., Cante, J., 2014. High-performance model reduction techniques in computational multiscale homogenization. Computer Methods in Applied Mechanics and Engineering 276, 149–189. URL: https://www.sciencedirect.com/science/article/pii/S0045782514000978, doi:10.1016/j.cma.2014.03.011.
Kanouté, P., Boso, D., Chaboche, J.e.a., 2009. Multiscale Methods for Composites: A Review. Archives of Computational Methods in Engineering 16, 31–75. URL: https://link.springer.com/article/10.1007%2Fs11831-008-9028-8#citeas, doi:10.1007/s11831-008-9028-8.
Kouznetsova, V., Brekelmans, W., Baaijens, F., 2001. An approach to micro-macro modeling of heterogeneous materials. Computational Mechanics 27, 37–48. URL: https://link.springer.com/article/10.1007/s004660000212, doi:10.1007/s004660000212.
Liu, Z., Bessa, M., Liu, W.K., 2016. Self-consistent clustering analysis: An efficient multi-scale scheme for inelastic heterogeneous materials. Computer Methods in Applied Mechanics and Engineering 306, 319 – 341. URL: http://www.sciencedirect.com/science/article/pii/S0045782516301499, doi:10.1016/j.cma.2016.04.004.
Liu, Z., Fleming, M., Liu, W.K., 2018. Microstructural material database for self-consistent clustering analysis of elastoplastic strain softening materials. Computer Methods in Applied Mechanics and Engineering 330, 547 – 577. URL: http://www.sciencedirect.com/science/article/pii/S0045782517307107, doi:10.1016/j.cma.2017.11.005.
Liu, Z., Wu, C., 2019. Exploring the 3d architectures of deep material network in data-driven multiscale mechanics. Journal of the Mechanics and Physics of Solids 127, 20 – 46. doi:10.1016/j.jmps.2019.03.004.
Liu, Z., Wu, C., Koishi, M., 2019. A deep material network for multiscale topology learning and accelerated nonlinear modeling of heterogeneous materials. Computer Methods in Applied Mechanics and Engineering 345, 1138 – 1168. doi:10.1016/j.cma.2018.09.020.
Lopez-Pamies, O., Castaeda, P.P., 2004. Second-order homogenization estimates incorporating field fluctuations in finite elasticity. Mathematics and Mechanics of Solids 9, 243–270. doi:10.1177/1081286504038467.
Lopez-Pamies, O., Goudarzi, T., Danas, K., 2013. The nonlinear elastic response of suspensions of rigid inclusions in rubber: Iia simple explicit approximation for finite-concentration suspensions. Journal of the Mechanics and Physics of Solids 61, 19–37. URL: https://www.sciencedirect.com/science/article/pii/S0022509612001925, doi:10.1016/j.jmps.2012.08.013.
MacQueen, J.B., 1967. Some methods for classification and analysis of multivariate observations.
Michel, J., Suquet, P., 2003. Nonuniform transformation field analysis. International Journal of Solids and Structures 40, 6937 – 6955. URL: http://www.sciencedirect.com/science/article/pii/S0020768303003469, doi:10.1016/S0020-7683(03)00346-9. special issue in Honor of George J. Dvorak.
Michel, J.C., Suquet, P., 2004. Computational analysis of nonlinear composite structures using the nonuniform transformation field analysis. Computer Methods in Applied Mechanics and Engineering 193, 5477–5502. URL: https://hal.archives-ouvertes.fr/hal-00088245.
Michel, J.C., Suquet, P., 2009. Nonuniform transformation field analysis: a reduced model for multiscale nonlinear problems in solid mechanics, in: Galvanetto, U., Aliabadi, F. (Eds.), Multiscale Modelling in Solid Mechanics - Computational Approaches. Imperial College Press, London.. Imperial College Press, pp. 159–206. URL: https://hal.archives-ouvertes.fr/hal-00367772. iSBN: 978-1-84816-307-2.
Michel, J.C., Suquet, P., 2016. A model-reduction approach in micromechanics of materials preserving the variational structure of constitutive relations. Journal of the Mechanics and Physics of Solids 90, 254 – 285. URL: http://www.sciencedirect.com/science/article/pii/S0022509616300928, doi:10.1016/j.jmps.2016.02.005.

Moulinec, H., Suquet, P., 1994. A fast numerical method for computing the linear and nonlinear mechanical properties of composites. Comptes rendus de l'Académie des sciences. Série II. Mécanique, physique, chimie, astronomie. URL: https://hal.archives-ouvertes.fr/hal-03019226.

Moulinec, H., Suquet, P., 1998. A numerical method for computing the overall response of nonlinear composites with complex microstructure. Computer Methods in Applied Mechanics and Engineering 157, 69–94. URL: https://www.sciencedirect.com/science/article/pii/S0045782597002181, doi:10.1016/S0045-7825(97)00218-1.

Nguyen, V.D., Noels, L., 2022a. Interaction-based material network: a general framework for (porous) microstructured materials. Computer Methods in Applied Mechanics and Engineering 389, 114300. doi:http://dx.doi.org/10.1016/j.cma.2021.114300.

Nguyen, V.D., Noels, L., 2022b. Micromechanics-based material networks revisited from the interaction viewpoint; robust and efficient implementation for multi-phase composites. European Journal of Mechanics - A/Solids 91, 104384. doi:https://doi.org/10.1016/j.euromechsol.2021.104384.

Nguyen, V.D., Wu, L., Noels, L., 2017. Unified treatment of microscopic boundary conditions and efficient algorithms for estimating tangent operators of the homogenized behavior in the computational homogenization method. Computational Mechanics 59, 483–505. URL: https://doi.org/10.1007/s00466-016-1358-z, doi:10.1007/s00466-016-1358-z.

Ostoja-Starzewski, M., Du, X., Khisaeva, Z., Li, W., 2007. Comparisons of the size of the representative volume element in elastic, plastic, thermoelastic, and permeable random microstructures. International Journal for Multiscale Computational Engineering 5, 73–82. doi:10.1615/IntJMultCompEng.v5.i2.10.

Peric, D., de Souza Neto, E.A., Feijóo, R.A., Partovi, M., Molina, A.J.C., 2010. On micro-to-macro transitions for multi-scale analysis of non-linear heterogeneous materials: unified variational basis and finite element implementation. International Journal for Numerical Methods in Engineering 87, 149 – 170. URL: http://dx.doi.org/10.1002/nme.3014.

Ponte Castaeda, P., 1992. New variational principles in plasticity and their application to composite materials. Journal of the Mechanics and Physics of Solids 40, 1757–1788. URL: https://www.sciencedirect.com/science/article/pii/002250969290050C, doi:10.1016/0022-5096(92)90050-C.

Ponte Castaeda, P., 1996. Exact second-order estimates for the effective mechanical properties of nonlinear composite materials. Journal of the Mechanics and Physics of Solids 44, 827–862. URL: https://www.sciencedirect.com/science/article/pii/0022509696000154, doi:10.1016/0022-5096(96)00015-4.

Ponte Castaeda, P., 2002a. Second-order homogenization estimates for nonlinear composites incorporating field fluctuations: Itheory. Journal of the Mechanics and Physics of Solids 50, 737–757. URL: https://www.sciencedirect.com/science/article/pii/S0022509601000990, doi:10.1016/S0022-5096(01)00099-0.

Ponte Castaeda, P., 2002b. Second-order homogenization estimates for nonlinear composites incorporating field fluctuations: Iiapplications. Journal of the Mechanics and Physics of Solids 50, 759–782. URL: https://www.sciencedirect.com/science/article/pii/S0022509601000989, doi:https://doi.org/10.1016/S0022-5096(01)00098-9.

Ri, J.H., Hong, H.S., Ri, S.G., . Cluster based nonuniform transformation field analysis: An efficient homogenization for inelastic heterogeneous materials. International Journal for Numerical Methods in Engineering n/a. URL: https://onlinelibrary.wiley.com/doi/abs/10.1002/nme.6696, doi:https://doi.org/10.1002/nme.6696, arXiv:https://onlinelibrary.wiley.com/doi/pdf/10.1002/nme.6696.

Saeb, S., Steinmann, P., Javili, A., 2016. Aspects of computational homogenization at finite deformations: A unifying review from reuss' to voigt's bound. Applied Mechanics Reviews 68. URL: https://asmedigitalcollection.asme.org/appliedmechanicsreviews/article-abstract/68/5/050801/443653/Aspects-of-Computational-Homogenization-at-Finite?redirectedFrom=fulltext, doi:10.1115/1.4034024.

Sepe, V., Marfia, S., Sacco, E., 2013. A nonuniform tfa homogenization technique based on piecewise interpolation functions of the inelastic field. International Journal of Solids and Structures 50, 725–742. URL: https://www.sciencedirect.com/science/article/pii/S0020768312004684, doi:10.1016/j.ijsolstr.2012.11.005.

Soldner, D., Brands, B., Zabihyan, R., Steinmann, P., Mergheim, J., 2017. A numerical study of different projection-based model reduction techniques applied to computational homogenisation. Computational Mechanics 60, 613–625. doi:10.1007/s00466-017-1428-x.

Wu, L., Adam, L., Doghri, I., Noels, L., 2017. An incremental-secant mean-field homogenization method with second statistical moments for elasto-visco-plastic composite materials. Mechanics of Materials 114, 180–200. URL: https://www.sciencedirect.com/science/article/pii/S0167663617300698, doi:10.1016/j.mechmat.2017.08.006.

Wu, L., Adam, L., Noels, L., 2021. Micro-mechanics and data-driven based reduced order models for multi-scale analyses of woven composites. Composite Structures 270, 114058. URL: https://www.sciencedirect.com/science/article/pii/S0263822321005183, doi:https://doi.org/10.1016/j.compstruct.2021.114058.

Wu, L., Noels, L., Adam, L., Doghri, I., 2013. A combined incremental-secant mean-field homogenization scheme with per-phase residual strains for elasto-plastic composites. International Journal of Plasticity 51, 80 – 102. URL: http://www.sciencedirect.com/science/article/pii/S0749641913001174, doi:10.1016/j.ijplas.2013.06.006.

Wulfinghoff, S., Cavaliere, F., Reese, S., 2018. Model order reduction of nonlinear homogenization problems using a hashinshtrikman type finite element method. Computer Methods in Applied Mechanics and Engineering 330, 149 – 179. URL: http://www.sciencedirect.com/science/article/pii/S0045782517306904, doi:10.1016/j.cma.2017.10.019.

Yvonnet, J., 2019. Computational Homogenization of Heterogeneous Materials with Finite Elements. Solid Mechanics and Its Applications, Springer, Cham. URL: https://link.springer.com/book/10.1007/978-3-030-18383-7, doi:10.1007/978-3-030-18383-7.

Yvonnet, J., He, Q.C., 2007. The reduced model multiscale method (r3m) for the non-linear homogenization of hyperelastic media at finite strains. Journal of Computational Physics 223, 341 – 368. doi:10.1016/j.jcp.2006.09.019.